T.R.

GEBZE TECHNICAL UNIVERSITY

GRADUATE SCHOOL OF NATURAL AND APPLIED SCIENCES

NEAR-FIELD HIGH RESOLUTION SAR IMAGING AND RCS CALCULATION WITH CONTINUOUS WAVE OR PULSE SIGNALS

OKYANUS TULGAR

A THESIS SUBMITTED FOR THE DEGREE OF

DOCTOR OF PHILOSOPHY

DEPARTMENT OF ELECTRONIC ENGINEERING

GEBZE

2016

T.R.

GEBZE TECHNICAL UNIVERSITY

GRADUATE SCHOOL OF NATURAL AND APPLIED SCIENCES

NEAR-FIELD HIGH RESOLUTION SAR IMAGING AND RCS CALCULATION WITH CONTINUOUS WAVE OR PULSE SIGNALS

OKYANUS TULGAR

A THESIS SUBMITTED FOR THE DEGREE OF DOCTOR OF PHILOSOPHY

DEPARTMENT OF ELECTRONIC ENGINEERING

THESIS SUPERVISOR

PROF. DR. AHMET ARİF ERGİN

GEBZE

2016

T.C.
GEBZE TEKNİK ÜNİVERSİTESİ
FEN BİLİMLERİ ENSTİTÜSÜ

SÜREKLİ DALGA VEYA DARBE İŞARETLERİ İLE YAKIN ALANDA YÜKSEK ÇÖZÜNÜRLÜKLÜ YAR GÖRÜNTÜLERİNİN OLUŞTURULMASI VE RKA HESABI

OKYANUS TULGAR
DOKTORA TEZİ
ELEKTRONİK MÜHENDİSLİĞİ ANABİLİM DALI

DANIŞMANI
PROF. DR. AHMET ARİF ERGİN

GEBZE
2016

GEBZE TEKNİK ÜNİVERSİTESİ	**DOKTORA JÜRİ ONAY FORMU**

GTÜ Fen Bilimleri Enstitüsü Yönetim Kurulu'nun 21/03/2016 tarih ve 2016/24 sayılı kararıyla oluşturulan jüri tarafından 01/04/2016 tarihinde tez savunma sınavı yapılan Okyanus TULGAR'ın tez çalışması Elektronik Mühendisliği Anabilim Dalında DOKTORA tezi olarak kabul edilmiştir.

JÜRİ

ÜYE (TEZ DANIŞMANI)	: Prof.Dr. Ahmet Arif ERGİN
ÜYE	: Prof.Dr. Yunus Emre ERDEMLİ
ÜYE	: Doç.Dr. Müjdat ÇETİN
ÜYE	: Yrd.Doç.Dr. Ali Köksal HOCAOĞLU
ÜYE	: Yrd.Doç.Dr. Koray KAYABOL

ONAY

Gebze Teknik Üniversitesi Fen Bilimleri Enstitüsü Yönetim Kurulu'nun

...../...../..... tarih ve ...../..... sayılı kararı.

İMZA/MÜHÜR

SUMMARY

In this work, algorithms for high resolution Synthetic Aperture Radar (SAR) imaging and Radar Cross Section (RCS) calculation with near-field/far-field measurements have been developed. These algorithms have been designed for three types of radar signals. These are Stepped Frequency Continuous Wave (SFCW), Stepped Frequency Pulse (SFP), and Chirp signals. These algorithms have mainly three stages. The first one is the calculation of range profiles with high resolution. The second one is the SAR image reconstruction with near-field/far-field measurements. The last one is the scattering center extraction and RCS calculation. In the first stage, the traditional range resolutions of SFCW, SFP, and chirp SAR have been improved significantly by applying the Matrix Pencil Method (MPM) to the sampled signals. The resulting algorithms make the range resolution independent of the bandwidth. In the same stage, another algorithm has been introduced in this work for the first time in the literature to compensate the Range-Doppler Coupling. This yields high resolution Doppler frequency estimation that does not depend on the pulse duration. Thus, the Doppler distortion in the range profiles can be reduced efficiently by using this algorithm. In the second stage, high resolution SAR images have been reconstructed by introducing some novel algorithms. These images have super resolution in both cross-range and range directions. Such that the relationship between the angular extent and cross-range resolution have been alleviated efficiently. In the last stage, first the scattering center features have been extracted from the SAR images and then used for the RCS calculation in the near-field. Thus, the far-field requirement in the RCS measurements is alleviated with this work. The simulation and measurement results show the efficacy of the developed algorithms.

Key Words: Matrix Pencil Method (MPM), Radar Cross Section (RCS), Range-Doppler Coupling, Synthetic Aperture Radar (SAR).

ÖZET

Bu çalışmada, yakın-alan/uzak-alan ölçüm verileri ile yüksek çözünürlüklü Yapay Açıklıklı Radar (YAR) görüntüleme ve Radar Kesit Alanı (RKA) hesabı için birçok algoritma geliştirilmiştir. Bu algoritmalar üç türden radar sinyal tipleri için tasarlanmıştır. Bunlar, Basamak Frekanslı Sürekli Dalga (BFSD), Basamak Frekanslı Darbe (BFD) ve Cıvıltı işaretleridir. Bu çalışmada tanıtılan algoritmalar genel olarak üç aşamaya sahiptir. Bunlardan ilki yüksek çözünürlüklü menzil profili hesabıdır. İkincisi, yakın-alan/uzak-alan ölçümler ile YAR görüntülemedir. Sonuncusu ise, saçılma merkezi çıkartımı ve RKA hesabıdır. İlk aşamada, geliştirilen yeni algoritmalar ile örneklenmiş sinyallere Matris Demet Metodu (MDM)'nu uygulayarak BSFD, BFD ve Cıvıltı işaretlerinin menzil çözünürlüğü önemli ölçüde iyileştirilmiştir. Ortaya konulan bu algoritmalar menzil çözünürlüğünü bant genişliğinden bağımsız hale getirmektedir. Aynı aşamada, menzil-Doppler etkileşimini telafi etmek için bir algoritma bu çalışmada literatürde ilk kez tanıtılmıştır. Bu algoritma darbe genişliğinden bağımsız şekilde yüksek Doppler çözünürlüğü sağlamaktadır. Bu sayede, menzil profillerindeki Doppler bozulması etkin şekilde azaltılmaktadır. İkinci aşamada tanıtılan özgün algoritmalarda ise YAR görüntüleri oluşturulmaktadır. Bu görüntüler hem çapraz-menzil hem de menzilde yüksek çözünürlüğe sahiptir. Öyle ki, açısal genişliğin çapraz-menzil üzerindeki etkisi azaltılmıştır. Son aşamada, öncelikle saçılma merkezi öznitelikleri YAR görüntülerinden çıkartılmış ve ardından yakın-alanda RKA hesabı için kullanılmıştır. Bu sayede, RKA ölçümleri için gerekli olan uzak-alan şartı hafifletilmiştir. Benzetim ve ölçüm sonuçları, geliştirilen bu algoritmaların etkinliğini göstermektedir.

Anahtar Kelimeler: Matris Demet Metodu (MDM), Menzil-Doppler Etkileşimi, Radar Kesit Alanı (RKA), Yapay Açıklıklı Radar (YAR).

ACKNOWLEDGEMENTS

Firstly, I would like to express my deep and sincere gratitude to my supervisor, Prof. Dr. Ahmet Arif ERGİN, who not only shared his profound scientific knowledge with me but also taught me great lessons of life. His support, suggestions and encouragement gave me the drive and will to complete this work.

Besides my advisor, I would like to thank the rest of my thesis committee: Prof. Dr. Yunus Emre ERDEMLİ and Asst. Prof. Dr. Köksal HOCAOĞLU for their insightful comments and encouragement to my thesis study.

My sincere thanks also goes to Kadir DURGUT, Ömer Faruk KİP, Hasan ERCİYAS and Gökhan KÖSE not only for their supports to my graduate study, but also for their immortal friendship in my life. I appreciate to my advisor Prof. Dr. Ahmet Arif ERGİN and Mr. DURGUT, who included me to their research team in the Open Field Electromagnetic Laboratory (ASEMLAB). The opportunities in this laboratory give me a practical perspective, which is the main framework of my thesis study.

Finally, I appreciate to my family, who have been given their supports patiently during my life. None of my academic achievements could be done without them.

TABLE of CONTENTS

	Page
SUMMARY	v
ÖZET	vi
ACKNOWLEDGEMENTS	vii
TABLE of CONTENTS	viii
LIST of ABBREVIATIONS and ACRONYMS	x
LIST of FIGURES	xv
LIST of TABLES	xvii
1. INTRODUCTION	1
1.1. Thesis Topic and Theoretical Background	1
1.2. Contribution of Thesis	4
2. FUNDAMENTALS of STEALTH TARGET DESIGN	6
2.1. Design Phases	8
2.2. Radar Cross Section and Direct Measurement	10
2.2.1. Terrain Clutters and Suppression Techniques	12
2.2.2. Range Profile Calculation	13
2.2.3. Calibration Method and RCS Calculation	16
2.3. Tomography-Based RCS Calculation	17
3. IMPROVED PENCIL BACK-PROJECTION METHOD	21
3.1. Formulation of the Problem	21
3.2. Range Profile Calculation with MPM	24
3.3. SAR Imaging with Back-Projection (BP)	28
3.3.1. Far-field BP	28
3.3.2. Near-field BP	29
3.4. Image Segmentation	30
3.4.1. Otsu Thresholding	31
3.4.2. Amplitude Extraction	32
3.5. Summary of the IPBP Method	33
3.6. Simulations	34
3.6.1. SAR Imaging and Segmentation	34

Page

3.6.2. RCS Extraction 37

3.7. Measurements 40

3.7.1. Range Profile Calculation with BPMPM 42

3.7.2. ISAR Imaging and Segmentation 44

3.7.3. RCS Extraction 46

4. HIGH RESOLUTION CHIRP ISAR IMAGING WITH NEAR-FIELD MEASUREMENTS 50

4.1. Formulation of the Signal Model 51

4.2. Matrix Pencil Method for Chirp Signals 54

4.3. ISAR Image Reconstruction 55

4.4. Simulations 56

5. ESTIMATING RADAR CROSS SECTION OF MOVING TARGETS WITH NEAR-FIELD MEASUREMENTS 62

5.1. Formulation of the Problem 62

5.2. Range Profile Calculation with MPM 64

5.3. ISAR Image Reconstruction 67

5.4. Simulations 68

6. CONCLUSION 72

7. FUTURE WORK 74

REFERENCES 75

BIOGRAPHY 78

APPENDICES 79

LIST of ABBREVIATIONS and ACRONYMS

Abbreviations and Acronyms		**Explanations**
x	:	Cross-range (m)
y	:	Range (m)
ϕ	:	Azimuth angle (degree)
θ	:	Elevation angle (degree)
$\mathbf{R}$	:	Line-of-sight vector
R_0	:	Measurement distance (m)
$R_{i,\theta}$	:	Distance between the antenna and i^{th} scattering center (m)
$\mathbf{r_i}$	:	Scattering center vector
M	:	Number of scattering centers
a_i	:	Complex reflectivity of ith scattering center
f	:	Measurement frequency (Hz)
C	:	Speed of light (m/s)
k_v	:	Spatial frequency variable (1/m)
Δk_v	:	Spatial frequency variable angular step size (1/m)
$f(x,y)$	:	Spatial target reflectivity function
h	:	Altitude of the flying object (m)
N	:	Number of frequency points
n'	:	Zero starting-time index
n	:	Time index
v	:	Modulus of the radial velocity (m/s)
$\tau_{i,\theta}$	:	Round-trip time (s)
B	:	Bandwidth (Hz)
z_i	:	Poles of the scattered waves
b_i	:	Complex amplitude of ith exponential
m	:	Baseband frequency variable index

L	:	Pencil parameter
$\dagger$	:	Moore-Penrose pseudo inverse
Q	:	Averaging index
$\mathbf{W(r)}$	:	Windowing function vector
X	:	Number of grids in the cross-range direction
Y	:	Number of grids in the range direction
Δx	:	Spatial step size in the cross-range direction (m)
Δy	:	Spatial step size in the range direction (m)
$p_{k,l,\alpha}$	:	Projected pixel positions onto the line-of-sight vector (m)
$n_{i,\alpha}(x_k, y_l)$	:	Vertical line that corresponds to the ith scattering center
$S_{ff}(x_k, y_l)$	:	Far-field SAR image
$\mathbf{P}$	:	Pixel vector
$\mathbf{R_0}$	:	Measurement distance vector
$c_{i,\alpha}(x_k, y_l)$	:	Circle arc that corresponds to the ith scattering center
$S_{nf}(x_k, y_l)$	:	Near-field SAR image
T	:	Threshold level
a_i'	:	Estimated reflectivity of the ith scattering center
x_i'	:	Estimated cross-range position of the ith scattering center (m)
y_i'	:	Estimated range position of the ith scattering center (m)
$\sigma(f, \theta)$	:	Radar cross section (m^2)
λ	:	Wavelength (m)
R_{ff}	:	Far-field requirement
D	:	Maximum linear dimension of the measured target (m)
$[\mathbf{F}]$	:	Data matrix
G	:	Antenna gain
P_t	:	Transmitted signal power
P_r	:	Received signal power
A_e	:	Effective antenna aperture
$\vec{p}$	:	Polarization vector of the back-scattered wave

$\vec{p}_r$	:	Polarization vector of the receiver antenna
$\mathbf{E}^{\mathrm{s}}$	:	Scattered electric field vector
$\mathbf{E}^{\mathrm{i}}$	:	Incident electric field vector
R_{un}	:	Unambiguous range
δ	:	Kronecker's delta function
$eig()$	:	Eigen value operator
$\angle$	:	Phase operator
T_k	:	Discrete range profile
$\odot$	:	Element-wise multiplication
ζ	:	Number of aspect angles
$h_g(x, y)$	:	Gray level image
t	:	Time variable
t'	:	Zero starting-time variable
Δt	:	Sampling interval in time domain
T_p	:	Pulse width
T_p'	:	Receiver pulse width
T_p^{cutt}	:	Cut-off pulse width
T_{pd}	:	Pulse width of the leading signal
T_r^{cutt}	:	Cut-off pulse repetition frequency
T_r	:	Pulse repetition period
f_c	:	Start frequency of Chirp signal
α	:	Chirp rate
f_d	:	Doppler frequency
f_d'	:	Estimated Doppler frequency
$s_{i,\theta}^{IF}$	:	Intermediate frequency signal
s_c	:	Clutter signal
Q	:	Averaging factor
n_o	:	Noise signal
ΔR	:	Range resolution

D_x	:	Spatial extent of the SAR/ISAR image in the cross-range direction
D_y	:	Spatial extent of the SAR/ISAR image in the range direction
T_{klm}	:	Circular projection of the pixel positions
$e_i(k,l)$	:	Square error
$\vec{e}_d$	:	Movement direction
dB	:	Decibel
dBm^2	:	Decibel square meter
APSW	:	Approximate prolate spheroidal wave
ASEMLAB	:	Açık saha slektromanyetik laboratuarı
BFD	:	Basamak frekanslı darbe
BFSD	:	Basamak frekanslı sürekli dalga
BP	:	Back-projection
BPMPM	:	Band pass matrix pencil method
CBP	:	Convolution back-projection
DOA	:	Direction of arrival
EM	:	Electromagnetic
FFT	:	Fast Fourier transform
FIR	:	Finite impulse response
ISAR	:	Inverse synthetic aperture radar
FT	:	Fourier transform
IF	:	Intermediate frequency
IFFT	:	Inverse fast Fourier transform
IFT	:	Inverse Fourier transform
IIR	:	Infinite impulse response
IPBP	:	Improved pencil back-projection
LMA	:	Levenberg-Marquardt algorithm
MDM	:	Matrix demet metodu
MNR	:	Multiplicative noise ratio
MPM	:	Matrix pencil method

MSE	:	Minimum square error
NIPBP	:	Near-field improved pencil back-projection
N-IPBP	:	Non-normalized improved pencil back-projection
NUFFT	:	Non-uniform fast Fourier transform
PBP	:	Pencil back-projection
PSF	:	Point spread function
PSR	:	Primary surveillance radar
PTRD	:	Projected target reflectivity density
RAM	:	Radar absorbing material
RAR	:	Real aperture radar
RF	:	Radio frequency
SAR	:	Synthetic aperture radar
SBR	:	Shooting and bouncing ray
SFCW	:	Stepped-frequency continuous wave
SFP	:	Stepped-frequency pulse
SNR	:	Signal to noise ratio
SPA	:	Signal processing algorithm
SVD	:	Singular value decomposition
VNA	:	Vector network analyzer
YAR	:	Yapay açıklıklı radar

LIST of FIGURES

Figure No:		Page
2.1:	Radar signal propagation.	6
2.2:	A traditional RCS measurement setup.	11
2.3:	Clutter effects in open-range measurements.	13
2.4:	Pyramidal RF absorbers.	13
2.5:	Range gating in range profile.	15
2.6:	Standard reflectors as calibration targets.	16
2.7:	RCS values at various aspect angles.	17
2.8:	Tomography-based RCS extraction diagram.	18
3.1:	SAR imaging setup for IPBP method.	21
3.2:	Flow chart of the IPBP method.	33
3.3:	Reconstructed ISAR images for simulation data.	35
3.4:	Reconstructed far-field SAR image via CBP by using the range profiles.	36
3.5:	Far-field RCS extraction results.	38
3.6:	Near-field RCS extraction results.	38
3.7:	Far-field RCS extraction results by using non-normalized IPBP (N-IPBP).	39
3.8:	Near-field RCS extraction results by N-IPBP.	39
3.9:	Target-1.	40
3.10:	Target-2.	41
3.11:	Target-2 dimensions.	42
3.12:	Calculated range profiles, -- denotes IFFT, x marker denotes BPMPM.	43
3.13:	Reconstructed ISAR images for target-1.	44
3.14:	IPBP ISAR images for target-2 with real measurements. The left one is in the far-field. The right one is in the near-field.	45
3.15:	Far-field CBP ISAR image for target-2.	45
3.16:	Extracted RCS values at 10 GHz frequency.	47
3.17:	Extracted RCS values for target-2 with far-field measurements.	47
3.18:	Extracted RCS values for target-2 with near-field measurements.	48
4.1:	Chirp ISAR measurement setup.	51

Figure No: **Page**

4.2: Calculated range profiles via FFT and MPM with 5 dB SNR value at aspect angle $\theta = 90°$. 58

4.3: A comparison between the range resolution of FFT and MPM. 59

4.4: Reconstructed ISAR images with the developed Chirp ISAR imaging algorithm for "Case-I and II". 59

4.5: Results of the developed algorithm in "Case-I and II" for the point targets located at $(0, 0)$ and $(0.3, -0.3)$. 60

4.6: Reconstructed ISAR images with the SNR value 0 dB. 61

5.1: The transmitted signal pocket. 65

5.2: Obtained range profiles, $\theta = 93°$. 69

5.3: Reconstructed ISAR images. 70

5.4: RCS graphs with 0 and 5 dB SNR values. 70

5.5: RCS graphs with 10 and 15 dB SNR values. 71

LIST of TABLES

Table No:		Page
3.1:	Coefficients and positions of the five point scatterers used to reconstruct far-field and near-field SAR images.	34
3.2:	Simulation times for the image reconstruction procedure.	36
4.1:	Coefficients and positions of the six point scattering centers used to reconstruct near-field ISAR images.	57

1. INTRODUCTION

1.1. Thesis Topic and Theoretical Background

Radar cross section (RCS) is a quantity of back scattered electromagnetic (EM) waves from an object in the far-field zone [1]. RCS is also a characteristic property of a target that signifies the stealth capability [1], [2]. This quantity should be as small as possible for a target so that it will not be detected by a radar. The shape or material of a target's body are the essential factors for the RCS pattern. These factors have been widely under consideration in RCS reduction studies. Highly reflective regions signify which sides of the body increase RCS. Scattering centers point out these regions and is the source of back radiation [3]. Once the scattering centers are determined, it will be said that which sides of the body should be changed or covered with a radar absorbing material (RAM). In addition to this, they have been also used for the far-field RCS calculation from the near-field measurements. Various algorithms were introduced for the scattering center extraction or SAR/ISAR imaging in the literature [4]-[15]. In these algorithms, mainly two problems arise. The first problem is concerned with the point spread function (PSF) of the imaging method and the second one is about the restrictions in a laboratory environment. The main goal of this thesis is to overcome these two problems by developing algorithms for the near-field high resolution SAR/ISAR imaging and RCS calculation.

The reason of the first problem is the imaging resolution. The polar format algorithm (PFA) is a SAR imaging technique, which interpolates the polar raster data to perform a two dimensional (2-D) or three dimensional (3-D) FFT by using Cartesian raster data [4]. This resample stage generates interpolation errors that decrease the image quality [5]. Besides, the range and cross-range resolutions of PFA are restricted by the bandwidth, angular extent, and center frequency [2]. A wider bandwidth or angular extent decreases the main lobe width of the PSF, and hence the position ambiguity. However, these parameters are restricted by the system hardware and target's complexity [3]. In order to avoid the resample stage, the coherent Doppler tomography was introduced in [5] by suggesting the use of circular convolution. This approach was applied to the near-field SAR imaging and RCS calculation in [6]. However, the required sampling rate of the approach was not given

clearly. According to [7], the sampling criteria of the circular convolution leads to small angular step sizes not to face aliasing problem. But, it is limited by some physical restrictions in a laboratory environment. Besides, unfeasible measurement times may occur in some real-life applications due to the large number of aspect angles needed. In addition, this method still requires bi-dimensional interpolation and some FFT processes that decrease the quality of the reconstructed image and the RCS accuracy. A direct RCS computation technique from a polar format image was also presented in [7]. This technique requires some FFT processes in the angular dimension. Therefore, the usability of this technique is restricted by the same reasons for the fast cyclical convolution. The last presented algorithm in [7] facilitates Cartesian imaging without reformatting. However, the modified downrange profiles were computed by performing FFT, which limits the range resolution and RCS computation accuracy. In [8], non-uniform fast Fourier transform (NUFFT) was used for near-field SAR imaging and RCS extraction. NUFFT requires a mixture of interpolation and fast Fourier transform (FFT) with oversampled frequency points that increase unfavorable effects of the PSF on the reconstructed image and RCS error. In [9], a tomographic formulation for the spot-light mode SAR imaging were introduced. Then, in [10], this formulation was adapted to SAR imaging from far-field measurement data by introducing the convolution back-projection (CBP) method. This approach was extended to the near-field SAR imaging in [11]. Inverse circular Radon transform was used in order to implement CBP for near-field SAR image formation and RCS extraction. CBP computes the range profiles in each aspect angle with a range resolution that is limited by the bandwidth or pulse duration. Then, the wavefronts obtained from the range profiles are superposed to form a SAR image. However, CBP suffers from a poor range resolution and generating artifacts around the scattering centers. The drawbacks of using FFT were pointed out in [12] by comparing the simulation and measurement results of such spectral estimation methods like periodogram, autoregressive linear prediction (ARLP), Music, etc. Each of them has some advantages or disadvantages related to side lobe level, main lobe width or speckles. Moreover, some of them have a target to clutter ratio (TCR) dependent resolution, for example Pisarenko, Music [12]. Matrix pencil method (MPM) is another spectral estimation method that facilitates better resolution than FFT likewise some methods in [12]. Especially, MPM gives super resolution since some conditions are satisfied (described in Section 3 and 4).

With this motivation, a pencil back-projection (PBP) method, which improves the outcome of the traditional CBP, was developed in [13] with the far-field approximation. First, forward-backward total least squares band-pass MPM was utilized in each aspect angle with approximate prolate spheroidal wave (APSW) functions for obtaining super resolution in range profiles. Then, BP was implemented with the inverse Radon transform for SAR image formation. It can be seen from the images that PBP has better resolution (only in the range direction) compared to the CBP results. In spite of the super resolution of the range profiles, the SAR image still has poor resolution in the cross-range direction. In fact, CBP and PBP have some cross-range resolutions that are increased by performing measurements in a wider angular window. However, the target's complexity leads to a limitation on the angular extent due to the complex EM scattering phenomena [3]. In [14], a finite impulse response (FIR) filter (instead of APSW functions) was used in the pre-filtering step of the PBP. The implementation results have better performance than the CBP algorithm. Another ISAR imaging algorithm was suggested in [15] using a 2-D MPM. It was assumed that if the angular extent is much smaller than one degree, ISAR images can be reconstructed with the far-field approximation via the 2-D MPM. But, this method limits the angular extent considerably.

There are several types of signaling techniques that affect the SAR imaging resolution. Using the single frequency pulse signals yields poor range resolution that depends on the pulse width [2]. Stepped-frequency continuous wave (SFCW) signals yield better range resolution than the single frequency pulse signals [2]. But, it leads to an increase in the computational burden and timing problems for some non-stationary targets. For the stepped-frequency pulse (SFP) signals, more than one pulse are needed to complete the frequency sweep [2]. Thus, another trade-off between the range resolution and measurement duration still exists. In order to avoid this trade-off, chirp signals have been widely used. The frequency bandwidth is scanned within only one pulse in the chirp signals [2]. Thus, it is possible to get high range resolution via chirp signals by consuming much lower measurement time than that needed by SFCW or SFP.

The efficacies of the imaging algorithms are often restricted by the physical restrictions in a laboratory environment. For instance, it is difficult to satisfy the far-field criteria due to the large distances needed [6]. Besides, rotating a realistic target (a ship or plane) to different aspect angles is another problem that increase the cost

for setting up the measurement system. The introduced methods in [4], [5], [9], [10], [13]-[15] require a far-field distance. Therefore, they can't be applied to spherical wave imaging. The given methods in [3], [6]-[8], [11] can be used for the near-field imaging, but the required system hardware restricts their efficacy. Therefore, it is often needed to have an algorithm that does not need a far-field distance or a laboratory environment.

1.2. Contribution of Thesis

In this thesis, three algorithms are introduced by addressing how to solve the problems related to the physical restrictions and imaging resolution. In Chapter 3, an improved pencil back-projection (IPBP) method is introduced for high resolution SFCW SAR imaging and RCS extraction from near-field measurements [16]. The PBP enhancement on the SAR imaging is improved with an image segmentation algorithm that reduces the undesired effects of the PSF and advances the RCS extraction accuracy. In addition, the BP stage of IPBP, which does not need a planar wave propagation, can be applicable to the spherical wave imaging. Thus, IPBP alleviates the far-field requirement from the measurements. Moreover, IPBP has the same range resolution with PBP, while it has better cross-range resolution than CBP and PBP. Thus, IPBP overcomes the problems related to the resolution and measurement distance.

ISAR imaging of a moving target reduces the measurement system's complexity remarkably. In Chapter 4, an algorithm for Chirp ISAR imaging has been developed for moving targets [17]. This approach does not need a laboratory environment and it can be performed for moving targets in their operational environments. For example, it is possible to extract the scattering centers of a ship by using measurement data obtained in the sea. Thus, it overcomes the problems related to the target supporting system and other physical restrictions. As another benefit of this algorithm, it makes the range resolution of Chirp radars independent of the bandwidth. Such that MPM is adapted to the Chirp radars in this thesis for the first time in the literature [17]. It yields better resolution than the traditional Chirp signaling approach. Furthermore, a novel ISAR imaging procedure is also introduced in this thesis [17]. This procedure yields clearer ISAR images compared to the PBP

and CBP results. Besides, it does not require a large angular extent to get high cross-range resolution. This novelty increases the efficacy of the algorithm for complex targets. However, the Doppler effect is neglected in the range profile calculation step [17]. This limits the target's radial velocity, and hence the efficacy of the approach. Actually, RCS calculation is not in the scope of [17]. In Chapter 5, another algorithm, which is an improved version of [17], is presented to determine the RCS of moving targets. This work introduces two novel approaches. First, Doppler frequencies (and radial velocities) are calculated with super-resolution that is not bounded by the pulse width or frequency bandwidth. This yields better accuracy compared to the FFT-based techniques. High resolution Doppler frequency estimation brings another novel approach for compensating the range-Doppler coupling. Thus, the limitations in [17] related to the target velocity is alleviated by this algorithm. After the compensation, range profiles and ISAR images are obtained with high resolution by applying the introduced procedures in [17] to the compensated signal. Then, the extracted scattering centers are used for the RCS determination with near-field measurements. It is another novelty in this work that the introduced approach does not need the far-field requirement or a laboratory environment for RCS calculations. Such that RCS values are determined in the operational environment of moving targets.

The following chapter gives fundamental information about designing a stealth target to emphasize the need for RCS measurements at short distances. In addition, the traditional measurement technique is summarized in the same chapter while explaining some main concepts such as range-profile, time or range-gating. The third chapter is organized to give the details of IPBP. A chirp ISAR imaging algorithm is explained in the fourth chapter by neglecting the Doppler effect. This effect is added to the calculations while introducing a novel algorithm in the fifth chapter. The efficacies of the developed algorithms are remarked in the conclusion. This thesis may be a framework for some current problems, which are given briefly in the seventh chapter.

2. FUNDAMENTALS of STEALTH TARGET DESIGN

Basically, an active radar compares the transmitted waves with the reflected ones in order to detect targets (see Figure 2.1) [2]. A passive radar only listens to incoming signals from a potential source such as a Mode A/C/S transponder [2]. In this work, only active radars are under consideration.

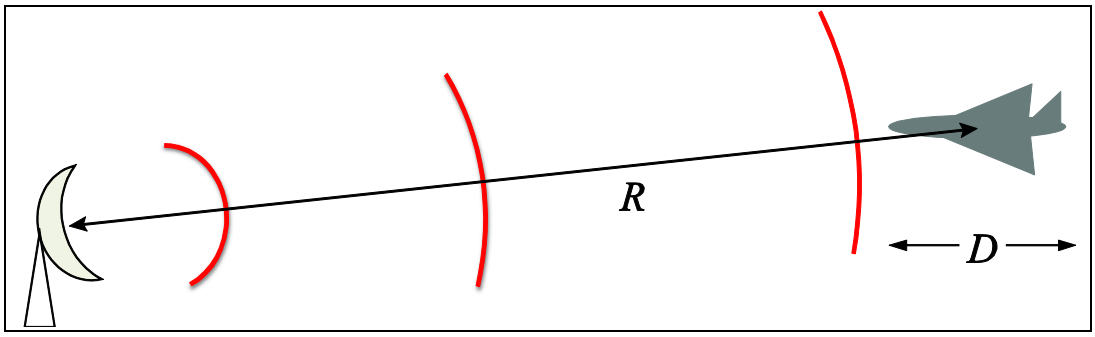

Figure 2.1: Radar signal propagation.

In Figure 2.1, an antenna emits the EM energy to the measurement space in order to induce surface currents on targets in the space. Then, these currents back radiate EM waves to various directions [18]. Some of them are collected by the receiver of radar. Then, the radar system processes the incoming signal to detect the target. This is the basis of active radar systems [2].

Assume that P_t is the power of transmitted signal. The radar signals propagate as spherical waves due to the three dimensional free-space Green's function [18]. Neglecting the antenna's directivity yields a signal power $P_t / 4\pi R^2$ for unit sphere area at the target's position [19]. Here, R is the distance between the antenna and target. In such radar systems, highly directive antennas are preferred to extend the maximum radar range and focus on the target's direction [2]. Besides, some type of radars, such as Primary Surveillance Radar (PSR) and Real Aperture Radars (RAR), have a cross-range resolution that is closely dependent to the half power beamwidth and hence the antenna gain. Using a directive antenna leads to an incident field power,

$$G(\theta, \phi, f) P_t / 4\pi R^2 . \tag{2.1}$$

Here, G is the antenna gain, f is the frequency, θ and ϕ are the elevation and azimuth angles, respectively [19]. The target reflects some portion of incident waves to various directions with a reflectivity $\sigma(\theta,\phi,f)$ that is called as the RCS [1]. Then, the power of back-scattered wave is reduced by the term $1/4\pi R^2$ due to the propagation loss. That yields a received signal power [19],

$$P_r = \sigma(\theta,\phi,f)\frac{G(\theta,\phi,f)P_t}{\left(4\pi R^2\right)^2}A_e, \tag{2.2}$$

where A_e is the effective antenna aperture that is equal to [19],

$$A_e = \frac{\lambda^2}{4\pi}G(\theta,\phi)\left|\vec{p}\cdot\vec{p}_r\right|. \tag{2.3}$$

Here, λ is the wavelength, $\vec{p}$ and $\vec{p}_r$ are the polarization vectors of the back-scattered waves and antenna, respectively. Thus, the received signal power can be written as,

$$P_r = \sigma(\theta,\phi,f)\frac{P_t G^2(\theta,\phi,f)\lambda^2}{(4\pi)^3 R^4 L_s}\left|\vec{p}\cdot\vec{p}_r\right|, \tag{2.4}$$

Here, L_s is the total insertion loss caused by the RF components in the radar system. This equation is called as the range equation in radar terminology [19]. It is clear from eqn. (2.4) that a less RCS yields lower received signal power.

The noise level of a radar system influences the required minimum signal power to detect a target. After receiving a reflected wave, the obtained signal contains thermal noises, which has a power proportional to the temperature and reciprocal to the pulse width. That is,

$$P_N = \frac{k_b T_k F_N}{\tau}, \tag{2.5}$$

where k_b is the Boltzmann constant, T_k is the effective temperature in Kelvin, F_N is the system's noise figure and τ is the pulse width. Dividing eqn. (2.4) with (2.5)

yields a signal-to-noise ratio (SNR),

$$\frac{P_r}{P_N} = \sigma(\theta,\phi,f)\frac{P_t G^2(\theta,\phi,f)\tau\lambda^2}{(4\pi)^3 k_b T_k F_N R^4 L_s}\left|\vec{p}\cdot\vec{p}_r\right|. \tag{2.6}$$

Radar systems sample the received signals to perform signal processing algorithms (SPA). All SPAs require a minimum SNR (SNR_m) level for efficient working. A received signal power leading to SNR < SNR_m does not give a reliable result after the SPA process. A lower RCS value reduces the SNR level of the received signal. This is the key information for the stealth technologies. A radar can only detect a target having a RCS value greater than $\sigma_m(\theta,\phi,f)$ at the target position R. This is the minimum RCS value for a radar as,

$$\sigma_m(\theta,\phi,f) = \mathrm{SNR}_m \frac{(4\pi)^3 k_b T_k F_N R^4 L_s}{P_t G^2(\theta,\phi,f)\tau\lambda^2\left|\vec{p}\cdot\vec{p}_r\right|}. \tag{2.7}$$

It is clear that reducing the target's RCS increases the stealth capability. For instance, two times lower RCS yields to a $\sqrt[4]{2}$ times lower maximum range that is required by the radar's SPA.

2.1. Design Phases

Designing a stealth target requires some phases that include RCS analysis with Computer Aided Design (CAD) models and real RCS measurements. The first stage is to draw a CAD model via a three dimensional (3D) CAD design software. The object is assumed to have a fully metallic object. Then, the scattered fields at various aspect angles and frequencies are calculated by using an appropriate EM solver. In order to calculate these fields, such solvers including full wave or asymptotic (known as high frequency) techniques have been widely used.

Full wave techniques were designed to solve the Maxwell equations with an appropriate discretization of object's geometry. Finite Difference Time Domain (FDTD) is an iterative method upon the time variable requiring a maximum 3D meshing size of $\lambda/10$ in each direction. Therefore, a huge number of mesh points are

required during the calculation of scattered fields from a realistic target such as a ship or plane. This leads to a heavy computational burden for RCS analyses. Method of Moments (MoM) is another technique that solves the electric or magnetic field integral equations with basis functions. The induced currents are calculated from the incident fields via some matrix operations. First, a matrix is constructed with the Green function. Then, the inverse of this matrix is multiplied with another matrix, which includes the incident fields. Finally, the scattered fields are calculated by using the calculated induced currents. It is clear that a wider object's dimension or frequency leads to huge matrix sizes. This makes it difficult to apply MoM to a large target because of the computational issues. Multilevel Fast Multipole Method (MLFMM) is also known as a full wave technique that is the fast version of MoM. These technique can be used for relatively larger targets compared to MoM. However, the computational issues related to memory and processor needs still occur during the RCS analysis for some realistic targets at high frequencies.

Instead of using of a full wave technique, some asymptotic methods have been preferred to obtain the result within a reasonable time. Physical optic (PO), geometric optic (GO), and shooting and bouncing rays (SBR) are known as asymptotic techniques. The matrix operations in MoM or MLFMM is approximated with a vector product to find the induced currents. Then, these currents are used for the calculation of scattered fields. This reduces the time or memory requirements, but decreases the accuracy. Because, the mentioned approximation leads to some error that becomes not to be negligible at low frequencies. This makes the PO method a high frequency technique. Besides, the multi-reflection effects cannot be added to the total scattered field. Therefore, the calculated RCS values may be lower than the result of real measurements. This is a deficiency of the usage of PO for complex targets. GO is another asymptotic technique that assumes the incident fields have an optical behavior. The direction of reflected fields are calculated with Snell's law. However, this assumption needs a high frequency. SBR is a ray tracing based technique that consists of both PO and GO. The incident plane waves are assumed to consist of independent rays. Each of them is sent toward the object. Then the hit points and reflection directions are calculated with GO. Finally, the scattered rays to the observation point are superposed to find total scattered field. This yields a better accuracy than PO thanks to the addition of multi-reflections to the scattered fields. In addition to this, range profiles, scattering centers and SAR/ISAR images can be

found within a reasonable time with SBR. These properties are crucial for the reduction of RCS. Especially, the scattering centers point out the strong reflection regions on the target's geometry. These regions can be covered with RSM to reduce the scattered field. In spite of the advantages of SBR, it calculates the scattered fields with an accuracy that is based on the PO and GO (with diffraction). Therefore, the accuracy of SBR is also limited by the frequency. This is the main reason of recognizing the SBR is another high frequency technique.

After the RCS analysis, the target is produced according to the CAD model to carry out the real RCS measurements. Although a computer-aided RCS analysis is useful for reduction of design cost and spent of time, it is clear that the scattering identity and stealth capabilities should be verified with real RCS measurements. This thesis addresses how to measure the scattering properties such as RCS, range profile and SAR/ISAR images.

2.2. Radar Cross Section and Direct Measurement

According to the antenna theory, the surface currents induced by the applied voltage to the antenna's RF connector lead to EM radiation. The shape and material properties of antenna determine the radiation pattern that varies with the aspect angle and frequency [20]. A similar situation arises for the target's scattering properties. Instead of applying a source voltage, the incident fields induce surface currents on the target's geometry. Then, they behave as the source of the back-scattered field. The energy of back-radiation depends on the strength (or gain) of induced currents. The phase and gain differences between these currents yield a radiation pattern that also depends on the aspect angle and frequency. Therefore, the target becomes to act as a directive antenna [18]. The radiation pattern of target is called as RCS [1].

RCS is the essential of stealth technologies, in which such studies have been carried out to reduce the back-scattered energy [21]. For instance, covering with RAM absorbs the incident electric field, and hence the strength of surface currents. This yields a smaller back-scattering and hence lower RCS values. Some geometrical improvements can be useful to reduce the power of echo signals. In order to determine the effectiveness of these studies, it is often required to measure the RCS with an appropriate technique. The definition of RCS is [21]

$$\sigma = \lim_{R \to \infty} 4\pi R^2 \frac{\left|\mathbf{E}^s\right|^2}{\left|\mathbf{E}^i\right|^2}, \tag{2.8}$$

where $\mathbf{E}^s$ is the scattered electric field from the object, $\mathbf{E}^i$ is the incident electric field at the target's position. Eqn. (2.8) says that a direct RCS measurement requires an infinite distance to obtain plane wave propagation. Of course, this distance can have a finite value in real applications. Therefore, the far-field criteria, $R > 2D^2/\lambda$, should be satisfied during the direct measurements. A simple diagram is given in Figure 2.2 to show a traditional RCS measurement setup [21].

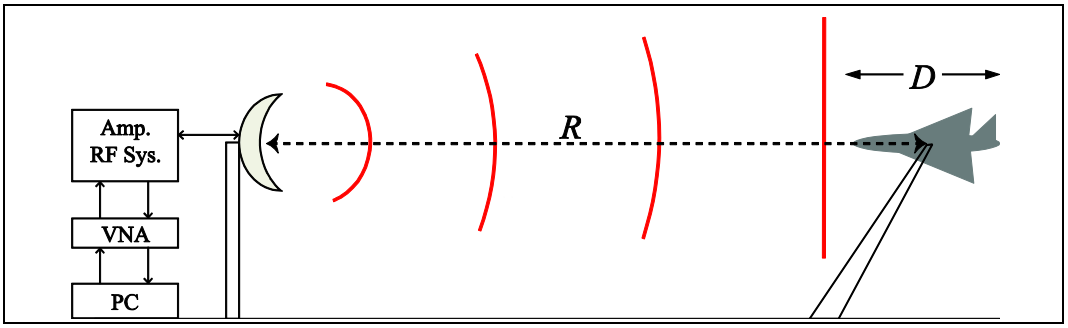

Figure 2.2: A traditional RCS measurement setup.

A pylon system supports and rotates the target to different azimuth (ϕ) and elevation (θ) angles. One or more directional antennas (generally parabolic reflectors with wideband horn feed) reside in the system to emit or collect the EM waves at each aspect angle and frequency. After setting up the trace parameters of VNA, it measures the S parameters such as S11, S21, S12, or S22 that depend on the structure of antenna system [21]. In order to increase the SNR level (and dynamic range) of received signal, the output power is amplified by an amplifier system. The interconnection between the antennas and VNA is done by using a RF sub system including coupler, switchers, circulator, limiters, low noise amplifier, etc.

Since the far-field criterion is satisfied, the incident electric fields at the target's position have a constant phase along a plane [21]. This yields a planar wave propagation as shown in Figure 2.2. This makes the target's radiation pattern independent to shape of the wavefront curvature and hence the measurement range. Note that RCS is the characteristic property of a target that does not change with the target's distance from a radar.

Once the measurement system is setup properly and assuming there are no clutter echoes coming to the antenna, the uncalibrated RCS values can be obtained directly by measuring the relevant S parameter in the frequency domain with VNA. After the proper calibration process (described in section 2.1.3), the target's calibrated RCS values will be measured without any further post-processing [21]. This type of RCS measurements are often carried out in open-range facilities due to the large distances needed [21]. Because, the required far-field distance for a realistic target requires a terrain that has a distance in the order of km. Unfortunately, clutter echoes become important in open-range measurements due to the ground reflections or other multipath propagation. These echoes reduce the measurement accuracy. Therefore, the clutter echoes should be removed from the received signal with a proper way. The next subsection describes how to overcome the clutter effects to enhance the measurement accuracy.

2.2.1. Terrain Clutters and Suppression Techniques

In the open-range measurements, received signals contain not only radiated energy from the target, but also clutter echoes and noise components [19], [21]. A simple diagram is given in Figure 2.3 to show the reason of clutter echoes. In this figure, the target is aligned in front of the antenna, having a physical dimension that is smaller than the main lobe width. This yields approximately a uniform signal power distribution across the target's geometry [21]. In Figure 2.3, there are also three buildings residing near the measurement terrain. Assume that the antenna is located at the origin of the Cartesian coordinate system and the buildings have some position vectors that have norms R_1, R_2, R_3. A range gating with an appropriate FIR or IIR filter having cut-off ranges $R_{c1} \leq R \leq R_{c2}$ yields a clear zone between R_{c1} and R_{c2} in the range domain. Thus, the clutter echoes having the ranges $R_1, R_2, R_3 \leq R_{c1}$ or $R_1, R_2, R_3 \geq R_{c2}$ are filtered out from data [21].

As another technique, the antenna's radiation pattern is designed specially according to the target's position. Such that each building vector has an angle outside the main lobe of the antenna's pattern. This reduces the incident energy to these buildings and received signal power. Such possible clutters (for instance, ground reflections) can be suppressed with this technique [21].

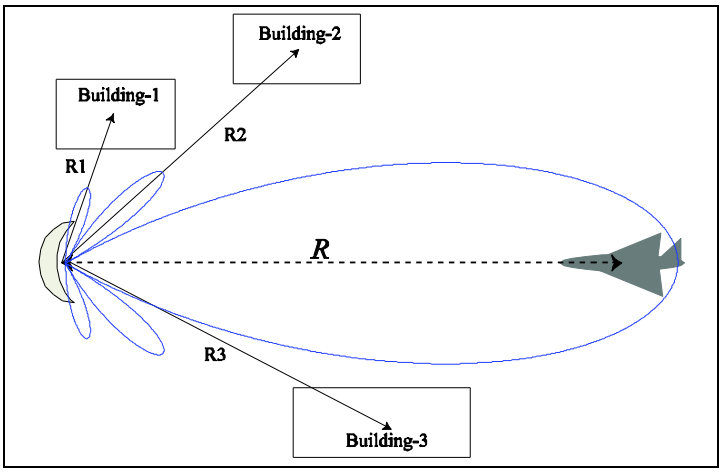

Figure 2.3: Clutter effects in open-range measurements.

It is possible that some clutter echoes may have indistinguishable distances with the measurement object. Therefore, a range gating may not sufficient to suppress these clutters. Moreover, some clutter objects may inside the main lobe of antenna. In order to fix this problem, RF absorbers (see Figure 2.4) are widely used in RCS measurements. However, the effective frequency band and the amount of absorbance is crucial in this case.

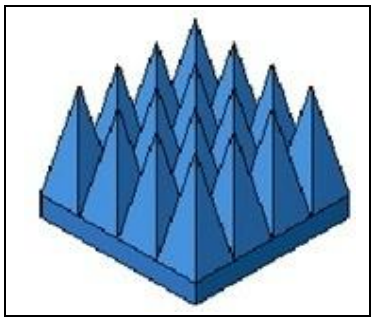

Figure 2.4: Pyramidal RF absorbers.

The range-gating requires a range profile calculation in each aspect angle [21]. The following section addresses how to obtain range profiles with a FFT-based traditional way.

2.2.2. Range Profile Calculation

The measured S parameter with VNA has a definition in the frequency domain [16],

$$S\left(\theta,\phi,k_v\right)=\int_x\int_y\int_z f\left(x,y,z\right)\cdot\frac{e^{-j2\pi k_v R_{\theta,\phi}}}{R_{\theta,\phi}^n}dzdydx,\ \ k_v=\frac{2f}{c}=\frac{2}{\lambda}, \tag{2.9}$$

where $f(x,y,z)$ is the target reflectivity model, $R_{\theta,\phi}$ is the range value corresponding to the look angles θ,ϕ. It can be assumed that a target is composed of a finite number of scattering centers, M. That leads to,

$$f(x,y,z)=\sum_{i=1}^{M}a_i\delta(x-x_i)\delta(y-y_i)\delta(z-z_i), \tag{2.10}$$

$$S\left(\theta,\phi,k_v\right)=\sum_{i=1}^{M}a_i\frac{e^{-j2\pi k_v R_{i,\theta,\phi}}}{R_{i,\theta,\phi}^n}, \tag{2.11}$$

$$R_{i,\theta,\phi}=\begin{cases}\sqrt{R_0^2+\rho_i^2+2R_0\left[(x_i\cos\phi+y_i\sin\phi)\sin\theta+z\cos\theta\right]}, & \text{for near-field}\\ R_0+(x_i\cos\phi+y_i\sin\phi)\sin\theta+z\cos\theta\qquad\qquad, & \text{for far-field}\end{cases} \tag{2.12}$$

where $n=1$ for the far-field and $n=2$ for the near-field EM wave propagation, $\rho_i^2=x_i^2+y_i^2+z_i^2$ and R_0 is the distance between the antenna and pylon system [16]. The range profile can be calculated by transforming $S\left(\theta,\phi,k_v\right)$ in eqn. (2.11) to the time domain with an appropriate way such as taking the inverse fast Fourier transform (IFFT) of it [16]. The inverse Fourier transform (IFT) of $S\left(\theta,\phi,k_v\right)$ leads to [22],

$$\begin{aligned}s(\theta,\phi,R)=IFT\left\{S\left(\theta,\phi,k_v\right)\right\}&=\int_{-\infty}^{\infty}S\left(\theta,\phi,k_v\right)e^{j2\pi k_v R}dk_v\\&=\sum_{i=1}^{M}a_i\delta(R-R_{i,\theta,\phi}).\end{aligned} \tag{2.13}$$

IFT requires infinite bandwidth and number of frequency points. Therefore, IFT can't be applied to real measurement data [22]. IFFT is a discrete version of IFT that leads to [22],

$$s(\theta,\phi,R)=IFFT\left\{S\left(\theta,\phi,k_v\right)\right\}=\sum_{i=1}^{M}a_i\mathrm{sinc}\left((R-R_{i,\theta,\phi})/\Delta R\right). \tag{2.14}$$

Here, ΔR is the range resolution that equals to $c/2B$, B is the bandwidth [19]. Assume that N is the number of frequency points, the maximum observable round-trip time is $\tau_{\max} = (N-1)/2B$ that leads to an unambiguous range $R_{\text{un}} = c(N-1)/4B$ [16]. Therefore, increasing the bandwidth turns to a reduction in the maximum observable range. In order to extend it, the number of samples should be also increased in the same time.

Figure 2.5 is an example for range profile, where four scatterers (three buildings and target) are residing. Assume that the fourth peak having a range value about 2610 m corresponds to the target's back-scattering. The other ones are the clutters caused by the buildings in Figure 2.3. The range-gating can be performed with an appropriate filter that covers the red colored dashed region in Figure 2.5 [21].

$$s_g(\theta,\phi,R) = IFFT\left\{S\left(\theta,\phi,k_v\right)\right\} \times w(R), \tag{2.15}$$

where s_g is the gated range profile, $w(R)$ is the filter function.

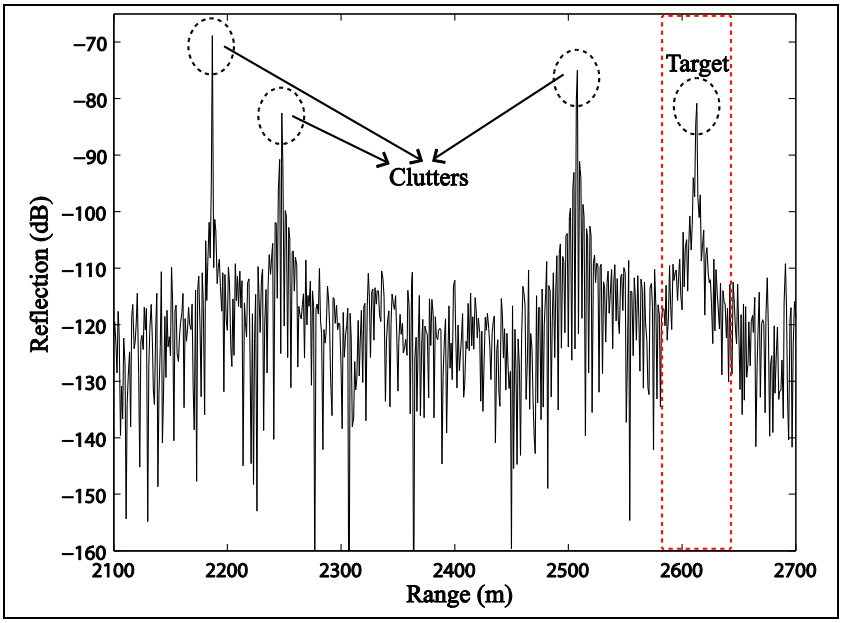

Figure 2.5: Range gating in range profile.

Taking the FFT of gated range profile yields uncalibrated RCS values for each frequency points [21]. That is,

$$\sigma_{\text{uncalibrated}}(\theta,\phi,f) = FFT\left\{s_g(\theta,\phi,R)\right\} = S\left(\theta,\phi,k_v\right) * W(f). \tag{2.16}$$

Here, $*$ denotes the convolution operation. In order to calibrate these RCS values, the following calibration method has been widely used in measurements [21].

2.2.3. Calibration Method and RCS Calculation

In practical applications, the path loss decreases received signal power with the fourth power of distance. In addition to this, RF devices also decrease the received signal level because of the insertion losses. The system can be calibrated totally with a reflector, which has well-known RCS values at different frequencies [16]. For this purpose, some standard reflectors such as dihedral, trihedral, sphere, etc. have been widely used as reference targets (see Figure 2.6) [21]. First, uncalibrated RCS values of the reference target, σ_{measured}, are obtained. Then, the total loss of measurement system can be calculated with $\sigma_{\text{loss}} = \sigma_{\text{reference}} - \sigma_{\text{measured}}$. Here, all RCS values are in the logarithmic scale (dBsm), $\sigma_{\text{reference}}$ is the theoretical RCS value of the reference target. Once the system loss has been determined, calibrated RCS values of a measurement target can be calculated by adding the system loss to the uncalibrated RCS values, $\sigma = \sigma_{\text{loss}} + \sigma_{\text{uncalibrated}}$ [21].

In Figure 2.6, sphere and trihedral reflectors are used for calibrating co-polarized measurements, while dihedral reflector is used for calibrating cross-polarized measurements [21]. The peak RCS values are given in (2.17).

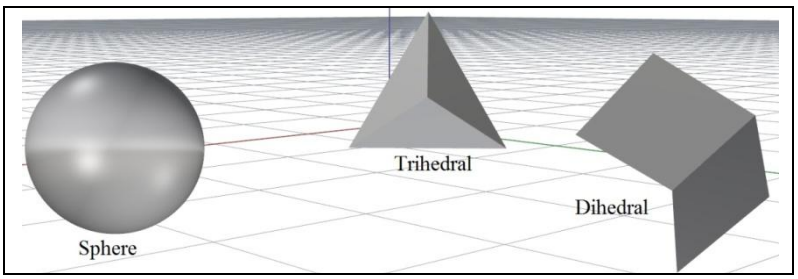

Figure 2.6: Standard reflectors as calibration targets.

$$\sigma_{\text{reference}} = \begin{cases} \pi r^2 & , \text{ for sphere (in optical region)} \\ 4\pi l^4 / (3\lambda^2), & \text{for trihedral} \\ 8\pi \left(\dfrac{ab}{\lambda} \right)^2 & , \text{ for dihedral} \end{cases} , \qquad (2.17)$$

where r is the sphere radius, l is the edge length of the trihedral, a and b are the lengths that correspond to the short and tall edges of dihedral [16], [21]. In Figure 2.7, RCS values in various look angles are depicted at 10 GHz frequency for 30 cm trihedral and dihedral reflectors. These values have been calculated by using SBR.

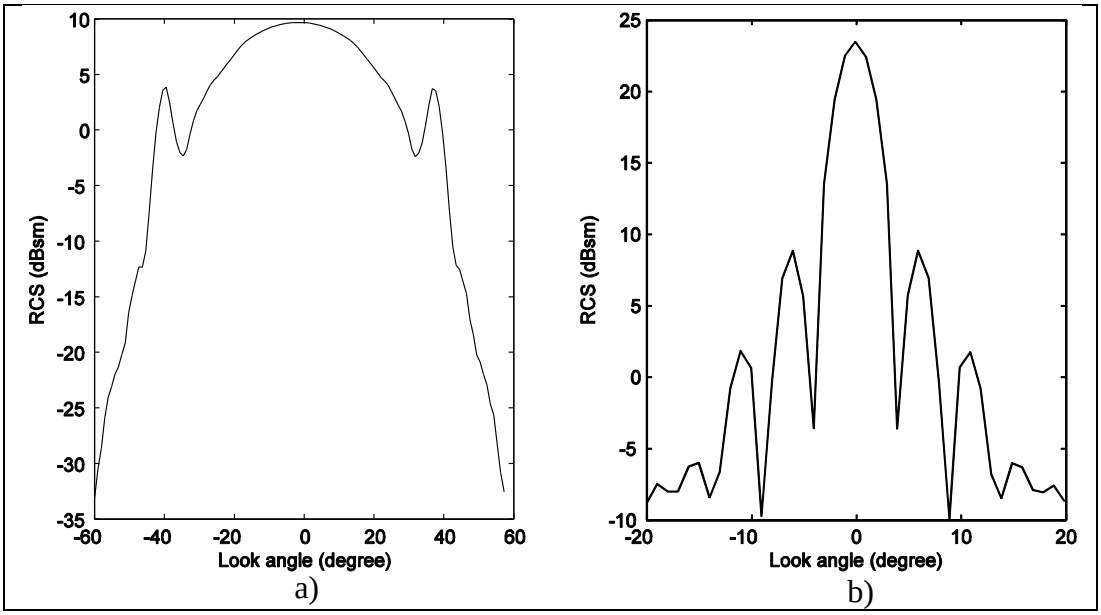

Figure 2.7: RCS values at various aspect angles. a) Linear-polarized for trihedral. b) Cross-polarized for dihedral.

2.3. Tomography-Based RCS Calculation

Due to the nature of RCS, a direct RCS measurement needs a far-field distance proportional to the frequency and square of target's dimension. But, it is difficult to satisfy this requirement due to the large distances needed. For instance, the far-field distance for a typical F-16 fighter is about 15 km for 10 GHz frequency. This distance can be larger for a ship having a dimension of about 40 m. Therefore, the required terrain and system hardware restrict the applicability of measurement setups for a realistic target. Moreover, measurements can be affected dramatically by the environmental issues such as rain, wind, ground reflections, etc. that reduce the open-range RCS measurement accuracy. Therefore, it is useful to predict far-field RCS values from near-field measurements. Algorithms for RCS extraction from near-field measurement data via SAR/ISAR imaging have been recently introduced [6]-[8],[16],[17]. The basis of these algorithms are depicted in Figure 2.8 [7], [16].

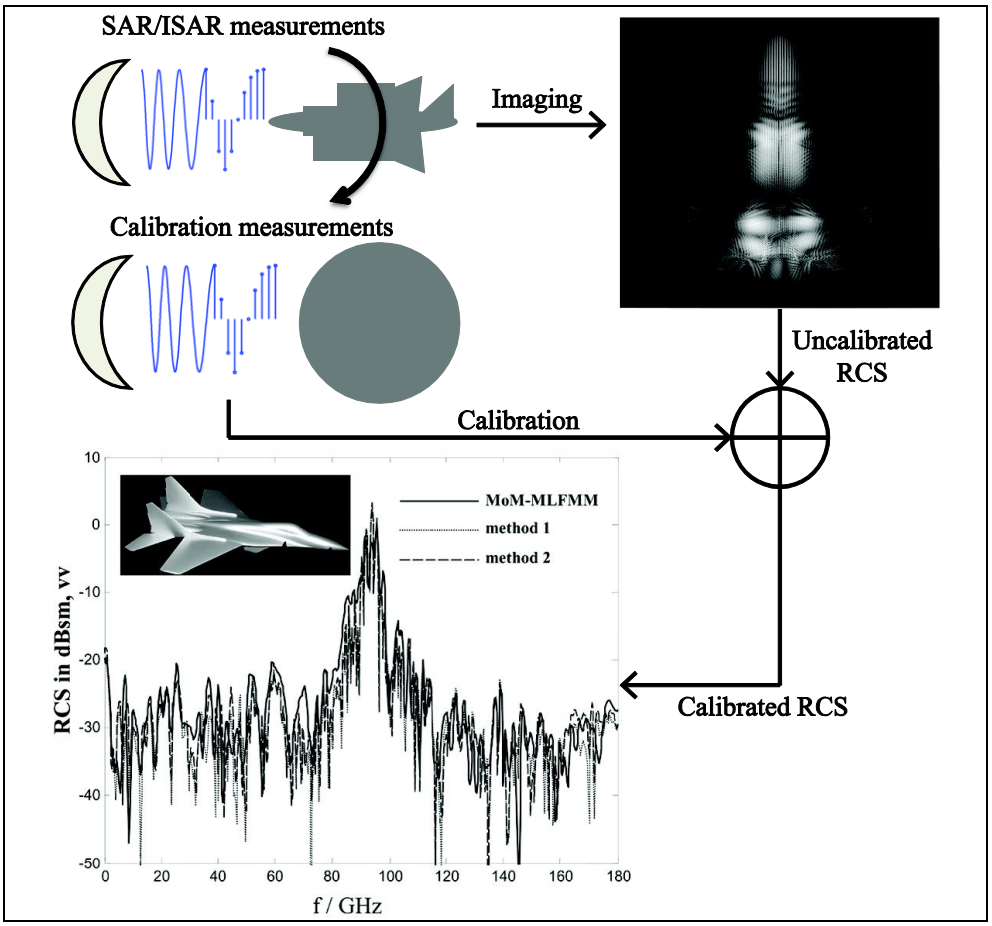

Figure 2.8: Tomography-based RCS extraction diagram.

In this type of RCS calculation, first, SAR/ISAR images are reconstructed from measurement data. Then, a proper scattering center extraction procedure, such as a Clean Algorithm or another image processing technique, is performed to obtain position and complex amplitude features. These scattering centers are used for the prediction of far-field EM propagation. After this prediction, uncalibrated far-field radiation patterns of target are calculated with the ratio between scattered and incident waves. They lead to the uncalibrated RCS values (as described in the next section) that are extracted from the near-field SAR/ISAR images. These values are calibrated by performing calibration measurements with a proper standard reflector. After these stages, the calibrated far-field RCS values are predicted from near-field measurements. The details of the high resolution SAR/ISAR imaging and RCS extraction will be explained in the following sections.

Assume that $S(x, y, z)$ is the three dimensional SAR/ISAR image consisting of the convolution between the PSF of the imaging method and each scattering center features for the measured target. That is,

$$I(x,y,z)=\sum_{i=1}^{M}a_i\int_{-\infty}^{\infty}\int_{-\infty}^{\infty}\int_{-\infty}^{\infty}P_S(x',y',z')\delta(x_i-x')\delta(y_i-y')\delta(z_i-z')dx'dy'dz' \quad (2.18)$$

Here, P_S is called as the PSF defining the imaging resolution. The first zero crossing points in the x, y, z dimensions are the resolutions $\Delta x, \Delta y,$ and $\Delta z,$ respectively. For instance, a Cartesian imaging via the PFA yields a PSF that has the main lobe widths reciprocal to the bandwidth and angular extents. The resolution cell (main lobe widths) and side lobe levels blur the scattering centers and create artifacts in the image. This issue reduces the image quality and hence the tomography-based RCS calculation accuracy. Therefore, some image processing procedures for the scattering center extraction are suggested in the literature [3], [16]. Novel procedures for the scattering center extraction are also introduced in this thesis. The details of them will be explained in the next section.

Assume that $a_i', x_i', y_i',$ and z_i are the scattering center features that are extracted from the SAR/ISAR image. The modulus of the scattered field can be written as follows under the far-field condition [16].

$$\begin{aligned} S\left(\theta,\phi,k_v\right) &\cong \sum_{i=1}^{M}a_i\frac{e^{-j2\pi k_v(R_0+(x\cos\phi+y\sin\phi)\sin\theta+z\cos\theta)}}{R_0^2}, \\ &= \frac{e^{-j2\pi k_v R_0}}{R_0^2}\sum_{i=1}^{M}a_i e^{-j2\pi k_v((x_i\cos\phi+y_i\sin\phi)\sin\theta+z_i\cos\theta)}. \end{aligned} \quad (2.19)$$

Putting eqn. (2.19) into (2.8) and using unity incident electric field leads to,

$$\sigma\left(\theta,\phi,k_v\right)=\lim_{R\to\infty}4\pi\left|\sum_{i=1}^{M}a_i e^{-j2\pi k_v((x_i\cos\phi+y_i\sin\phi)\sin\theta+z_i\cos\theta)}\right|^2. \quad (2.20)$$

As seen in eqn. (2.20), the parameter R tends to infinity. This leads to a planar wave propagation at the target's position. Of course, this distance is not feasible for real applications. Therefore, this requirement has been satisfied approximately with the far-field condition $R>2D^2/\lambda$ that drops the limit in eqn. (2.20). This yields an uncalibrated RCS formula as follows.

$$\sigma_{\mathrm{dB}}\left(\theta,\phi,k_{\mathrm{v}}\right)=20\log_{10}\left|\sum_{i=1}^{M}a_i e^{-j2\pi k_{\mathrm{v}}((x_i\cos\phi+y_i\sin\phi)\sin\theta+z_i\cos\theta)}\right|. \tag{2.21}$$

After obtaining the uncalibrated RCS values, a proper calibration measurement is performed to predict far-field RCS values.

This type of RCS calculation needs the scattering center features indexed with i. Therefore, a better feature extraction increases the RCS calculation accuracy as demonstrated in the next section. Because of this relationship, a clearer SAR/ISAR imaging yields a better feature extraction, and hence less RCS error. This is the main reason of developing high resolution SAR/ISAR imaging algorithms in this thesis. PBP uses far-field measurement data due to the plane wave approximation. The subject of the following chapter is to extend the efficacy of PBP to near-field case and RCS prediction at short distances.

3. IMPROVED PENCIL BACK-PROJECTION METHOD

The IPBP method is a high resolution SAR/ISAR imaging and RCS extraction algorithm that was introduced in [16]. The main differences between the PBP and IPBP are about the far-field requirement, cross-range resolution and RCS extraction. The details of this method is given next.

3.1. Formulation of the Problem

The SAR imaging geometry is illustrated in Figure 3.1.

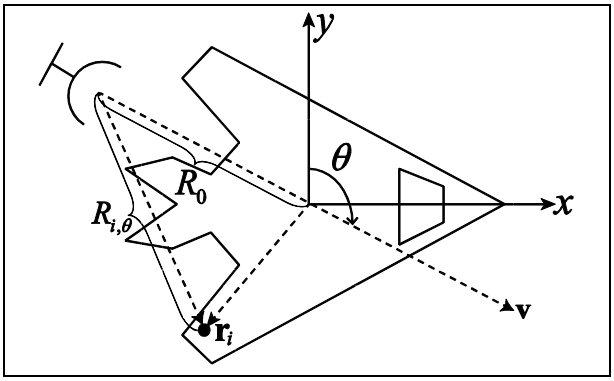

Figure 3.1: SAR imaging setup for IPBP method.

A monostatic radar antenna turns around the object with the aspect angle θ and the line of sight vector $\mathbf{v}$. The distance between the antenna and target coordinate system is R_0. Measured data can be expressed as

$$F\left(\theta, k_v\right) = \int\int f\left(x, y\right) \frac{e^{-j2\pi k_v R}}{R^n} dydx, \tag{3.1}$$

where k_v is a spatial frequency variable that has the value of $k_v = 2f/c$, here f and c are the measurement frequency and the speed of light, respectively, $f(x, y)$ is the spatial target reflectivity function, and R is the distance from the antenna to the point (x, y) [13]. The variable n should be selected as $n = 1$ for the far-field and $n = 2$ for the near-field case [8], [13].

In this work, it is assumed that point scattering centers, which are composed of linear combination of two dimensional Kronecker's delta functions, form the target reflectivity model. That is,

$$f\left(x,y\right)=\sum_{i=1}^{M}a_i\delta\left(x-x_i\right)\delta\left(y-y_i\right), \tag{3.2}$$

where M is the total number of scattering centers, a_i is the reflectivity of the ith scatterer, x_i and y_i are the cross-range and range positions (for $\theta=0°$) in the two dimensional Cartesian space, respectively [13]. By substituting the point scatterer model given in (3.2) into (3.1), the discrete scatterer case of (3.1) is obtained as,

$$F_d\left(\theta,k_v\right)=\sum_{i=1}^{M}a_i\frac{e^{-j2\pi k_v R_{i,\theta}}}{R_{i,\theta}^n}. \tag{3.3}$$

In (3.3), $R_{i,\theta}$ is the distance between the antenna and the ith scatterer. This scalar quantity can be written for the far-field and near-field cases as [8], [13],

$$R_{i,\theta}=R_0+x_i\sin\theta+y_i\cos\theta \tag{3.4}$$

$$R_{i,\theta}=\sqrt{R_0^2+x_i^2+y_i^2+2R_0\left(x_i\sin\theta+y_i\cos\theta\right)}. \tag{3.5}$$

The first expression can be used for only the plane wave excitation. In this case, the denominator of (3.3) can be taken as approximately equal to R_0. The second expression, (3.5), is a general representation that can be used for both far-field and near-field cases.

The target reflectivity function can be calculated with the collected data as [13]

$$f\left(x,y\right)=\int_{\theta}\left(\int_{k_v}R_{i,\theta}^n F_d\left(\theta,k_v\right)e^{j2\pi k_v R}\left|k_v\right|dk_v\right)d\theta. \tag{3.6}$$

The inner integral of (3.6) corresponds to the range profile that can be calculated with FFT with respect to the discrete spatial frequency variable k_v at each aspect angle θ. But FFT suffers from Gibbs phenomena and poor range resolution because

of the limited frequency bandwidth and discrete range domain. For the FFT process, the range resolution has the formula $\Delta R = c/(2B)$, where B is the measurement bandwidth. For the tomography-based RCS extraction algorithms, the accuracy of the calculations is closely related to the range resolution at each aspect angle. In order to increase the range resolution to enhance image quality (and RCS extraction accuracy), B must be increased for the FFT process. But, the measurement bandwidth is limited in real life applications because of the hardware limitations and sampling issues in the range domain. Another problem for the FFT process is the leakage between scattering points. This problem arises due to the representation of each scattering center with the impulse response of a windowing function that is widely used for decreasing the unfavorable impacts of the band limited data on the discrete transformation space by balancing the main lobe width and side lobe levels [22]. Band-pass MPM (BPMPM) is utilized in this work to calculate the range profile at each aspect angle with super resolution even if band limited data is used. The outer integral in (3.6) can be calculated with BP for both far-field and near-field cases. The outcome of the BP process is the target reflectivity function $f(x, y)$ that indicates a two dimensional complex valued image. For the ith scatterer, the reconstructed SAR image contains *estimated* values of the reflectivity, the cross-range, and range position, which are represented with the symbols a_i', x_i', y_i', respectively.

The measured data is proportional to the ratio between amplitudes of the scattered and incident fields under the far-field condition, and can be represented in a phasor form as,

$$F_d\left(\theta, k_v\right) \cong \frac{e^{-j2\pi k_v R_0}}{R_0} \sum_{i=1}^{M} a_i e^{-j2\pi k_v (R_0 + x_i \sin\theta + y_i \cos\theta)}. \tag{3.7}$$

After the calibration, RCS values can be calculated with the estimated scattering centers by substituting (3.7) into (2.8) as (3.8),

$$\sigma\left(f, \theta\right) = \sigma_{\text{loss,dB}} + \left| \sum_{i=1}^{M} a_i' e^{-j4\pi \frac{f}{c}\left(x_i' \sin\theta + y_i' \cos\theta\right)} \right|_{\text{dB}}^{2}. \tag{3.8}$$

3.2. Range Profile Calculation with MPM

MPM allows the extraction of complex amplitudes and poles of each exponent with super resolution from band limited measurement data [24]. MPM operates on the k_v-space and does not require discretization of the range domain, which facilitates extraction of range profiles without having any issues in terms of the range resolution.

In the range profile calculation step of the developed algorithm, SFCW SAR signal processing is assumed. Thus, the collected data have the form [13],

$$F_m = F_d\left(\left(m + n_{\min}\right)\Delta k_v\right) = \sum_{i=1}^{M} r_i z_i^m + w_m \tag{3.9}$$

$$r_i = b_i z_i^{n_{\min}},\ \ z_i = e^{-j2\pi R_{i,\theta}\Delta k_v}, \tag{3.10}$$

where m and n are the sampling indices of the data such that,

$$m = n - n_{\min} \in \{0,1,\ldots,n_{\max} - n_{\min}\}, \tag{3.11}$$

as described in [13], $n_{\min}$ and $n_{\max}$ are the indices that correspond to the minimum and maximum frequency values for the given frequency band, Δk_v is the sampling step size, w_m is the noise component of data, b_i is the complex amplitude of the ith scattering center exponential. For the SFCW SAR signal processing, sampling in the frequency domain should satisfy the Nyquist criteria

$$B \le \frac{c\,(N-1)}{4\max\limits_{i,\theta}\left\{R_{i,\theta}\right\}}, \tag{3.12}$$

in order to find range profiles that correspond to the phase interval $[-\pi,\ \pi]$ (will be described later). The variable N in (3.12) is the number of frequency points. Thus, the minimum and maximum measurable distances are,

$$R_{\min} = -c(N-1)/(4B),\quad R_{\max} = c(N-1)/(4B), \tag{3.13}$$

respectively. Equation (3.12) and the range resolution formula can cause heavy computational burden due to the large distances required by the far-field condition. For example, a typical target might have the largest linear dimension of 15 m. According to the far-field approximation, $R_0 > 2D^2/\lambda$, the far-field requirement for this target is 15 km at 10 GHz. If desired range resolution for IFFT is 1 cm, the required number of samples is 30×10^5, which causes a large computation time as well as hardware problems for the computer and network analyzer. In addition, this range resolution requires 15 GHz bandwidth while MPM is not directly bounded in terms of bandwidth to produce super range resolution. Hence, the same or better resolution may be obtained by choosing $B = 15$ MHz and 3001 samples with MPM. This demonstrates the importance of obtaining range profiles with super resolution by using MPM in narrow bandwidth.

The MPM is described next. Assume a matrix $[\mathbf{F}]$ having the form,

$$[\mathbf{F}] = [\mathbf{f}_0\ \mathbf{f}_1 \ldots \mathbf{f}_L], \quad \mathbf{f}_n = [F_n\ F_{n+1} \ldots F_{N-L+n-1}]^T, \tag{3.14}$$

where L is the pencil parameter that should be between $N/3$ and $N/2$ for efficient noise filtering [13]. Singular value decomposition (SVD) of $[\mathbf{F}]$ is,

$$[\mathbf{F}] = [\mathbf{U}][\Sigma][\mathbf{V}]^H. \tag{3.15}$$

The singular value matrix $[\Sigma]$ has a diagonal form that contains all singular values in descending order. The largest M singular values correspond to the number of the scattering centers that must satisfy $M \le L \le N - M$ [24].

Let $[\mathbf{F}']$ be a matrix that is reproduced with the M dominant singular values for the noise filtering [25]. The poles of $F_d(\theta, k_v)$ can be determined as,

$$z_i = eig\left([\mathbf{F}_1']^\dagger [\mathbf{F}_2']\right);\ [\mathbf{F}_1'] = [\mathbf{f}_0'\ \mathbf{f}_1' \ldots \mathbf{f}_{L-1}']_{(N-L)\times L},\ [\mathbf{F}_2'] = [\mathbf{f}_1'\ \mathbf{f}_2' \ldots \mathbf{f}_L']_{(N-L)\times L}, \tag{3.16}$$

where $eig(\cdot)$ is the eigen value operator and dagger $(\dagger)$ denotes the Moore-Penrose pseudo inverse.

The range value of the ith scattering center at aspect angle θ can be found with,

$$R_{i,\theta} = -\angle z_i / (2\pi \Delta k_v), \quad i = 1, 2, \ldots, M, \tag{3.17}$$

where $\angle z_i$ denotes the phase of the ith pole. Substituting $\Delta k_v = 2B/(c(N-1))$ in the previous formula leads to,

$$\angle z_i = -4\pi R_{i,\theta} B / (c(N-1)). \tag{3.18}$$

According to (3.10), the poles, z_i, are 2π periodic, that causes an infinite number of solutions. But, the expressions for the $R_{\min}$ and $R_{\max}$ guarantee evaluation of a unique range for each scatterer. By substituting the measurable ranges into the expression of $\angle z_i$, the phase interval can be shown to be $\angle z_i \in [-\pi, \pi]$.

Once the poles, z_i, have been extracted, the (noiseless version of) (3.9) can be inverted as

$$\left[r_1, r_2, \ldots, r_M\right]^T = \left(\left[\mathbf{Z}\right]^T\right)^{\dagger} \left[F_0, F_1, \ldots, F_{N-1}\right]^T, \tag{3.19}$$

in order to find r_i. Here, $\left[\mathbf{Z}\right]$ is the Vandermonde matrix containing the obtained poles z_i'. That is,

$$\left[\mathbf{Z}\right] = \begin{bmatrix} 1 & 1 & \cdots & 1 \\ z_1' & z_2' & \cdots & z_M' \\ z_1'^2 & z_2'^2 & \cdots & z_M'^2 \\ \vdots & \vdots & \cdots & \vdots \\ z_1'^{N-1} & z_2'^{N-1} & \cdots & z_M'^{N-1} \end{bmatrix}_{(N-1)\times M}. \tag{3.20}$$

Then, using (3.10) and the relation between (3.3) and (3.9), the complex amplitudes, b_i, and the reflectivity, a_i, of each scattering center can be calculated as,

$$b_i = r_i / (z_i^{n_{\min}}), \quad a_i = b_i R_{i,\theta}^n, \quad i = 1, 2, \ldots, M. \tag{3.21}$$

The noise components and clutter in the measurement data may cause incorrect calculation of the total number of scattering centers after the SVD process. This, in turn, leads to incorrect calculation of the poles and complex amplitudes. In order to

decrease the effect of noise in the SVD process, the BPMPM was developed in [26], in which both infinite impulse response (IIR) and FIR prefiltering techniques were considered. However, the use of a gating process that will be described next obviates the need to apply the costly filtering process described in [26].

Scattering center features cannot be calculated directly by using (3.16) and (3.19) because of some potential backscattering (clutter) in the incoming signal due to the open range measurements. A gating process in the range domain with an appropriate windowing function can be applied to the data in order to eliminate the effects of clutter and noise components outside of the range region of interest. Assume that W_k is the windowing function. The discrete range profile, T_k, for each aspect angle can be calculated using IFFT as,

$$T_k = N\sum_{n=0}^{N-1} F_n\, e^{j2\pi\frac{n}{N}k}\,;\; k = 0,1,\ldots,N-1. \tag{3.22}$$

The range-gated data (i.e., the prefiltered data in [26]) can be produced with,

$$[\mathbf{\Gamma}] = FFT\left\{[\mathbf{T}]\otimes[\mathbf{W}]\right\}. \tag{3.23}$$

These vectors are defined as,

$$[\mathbf{\Gamma}] = [\Gamma_0, \Gamma_1, \ldots, \Gamma_{N-1}],\quad [\mathbf{T}] = [T_0, T_1, \ldots, T_{N-1}],\quad [\mathbf{W}] = [W_0, W_1, \ldots, W_{N-1}], \tag{3.24}$$

and $\otimes$ denotes the element-wise multiplication for the related vectors. The gating process causes a frequency shift because of the phase delay of W_k. Fortunately, it is possible to recover the data points by a back-shift process. Assume that τ is the group delay of W_k. If the windowing function has a linear phase response, the group delay is not a function of frequency, which makes possible the usage of the back-shift operation as $\Gamma'_{j-\tau} = \Gamma_j$; $j = \tau, \ldots, N-1$. The complex amplitudes can be found by using $[\mathbf{\Gamma}']$ instead of $[\mathbf{F}]$ by using the formula,

$$[r_1, r_2, \ldots, r_M]^T = \left([\mathbf{Z}]^T\right)^{\dagger} [\Gamma'_0, \Gamma'_1, \ldots, \Gamma'_{N-1-\tau}]^T. \tag{3.25}$$

The back-shift operation decreases the total number of data points by τ. It means that according to (3.12), this procedure may cause the degeneration of the Nyquist criteria if the group delay is greater than a specific value. Hence, the order of the windowing function should be selected small enough in order not to face any sampling issues.

3.3. SAR Imaging with Back-Projection (BP)

Back-projection is an image formation algorithm that directly works with polar format data. Therefore, BP does not require polar-to-Cartesian interpolation and is devoid of spectral domain interpolation and near-field imaging problems. In the far-field zone, it is assumed that planar wave propagation exists in the measurement space. Thus, the projected target reflectivity density (PTRD) function along the line of sight direction, $\mathbf{v}$, is the sum of Radon transforms of each scattering center as described in [13]. In other words, inverse Radon transform can be applied to the range profiles in order to form the SAR image. But in the near-field case, the range values denote the radii of circles whose origins are the antenna position. Hence, circular inverse Radon transform should be carried out in order to form the near-field SAR image as described in [11]. The far-field and near-field BP techniques used in this work will be explained next.

3.3.1. Far-field BP

Assume that the reconstructed SAR image $S(x,y)$—which is akin to the $f(x,y)$ function in (3.6)—has X and Y grids, Δx and Δy resolutions in the cross-range and range dimensions, respectively, at the target coordinate system. The PTRD function for the αth look angle θ_α can be produced via range correction for the ith scatterer as $v_{i,\alpha} = R_{i,\theta_\alpha} - R_0$. The projection of the pixel position (x_k, y_l) onto the line of sight along the vector $\mathbf{v}$ is $p_{k,l,\alpha} = x_k \sin\theta_\alpha + y_l \cos\theta_\alpha$, where the positions and aspect angles are given as,

$$x_k = x_{\min} + (k-1)\Delta x, \quad \mathrm{y}_l = y_{\min} + (l-1)\Delta y, \quad \theta_\alpha = \theta_{\min} + (\alpha-1)\Delta\theta \quad (3.26)$$

The indices for the x and y take the values $k=1,2,\ldots,X$, $l=1,2,\ldots,Y$ and the aspect angle index is in the range $\alpha=1,2,\ldots,\zeta$, where ζ is the number of measurement angles. Far-field BP is the superposition of the lines that are orthogonal to the $\mathbf{v}$ direction with the complex amplitudes at each position point in the range profiles. For the ith scatterer, the orthogonal line at aspect angle θ can be drawn in the image with the nearest neighbor interpolation as,

$$n_{i,\alpha}\left(x_k, y_l\right)=\begin{cases} a_i & \text{if } \left|p_{k,l,\alpha}-v_{i,\alpha}\right|<\Delta l \\ 0 & \text{otherwise} \end{cases}, \tag{3.27}$$

where $\Delta l=\min\left(\Delta x,\Delta y\right)/2$. The far-field SAR image can be reconstructed with the superposition of (3.27) over all incidence angles as,

$$S_{ff}\left(x_k, y_l\right)=\frac{1}{\zeta}\sum_{i=1}^{M}\sum_{\alpha=1}^{\zeta} n_{i,\alpha}\left(x_k, y_l\right). \tag{3.28}$$

3.3.2. Near-field BP

Assume that each pixel point (located at $\mathbf{p}$) has a complex amplitude and let $\mathbf{R}_0$ specify the vector from the antenna to the origin of the target coordinate system. The radius of the circle that passes through each pixel position is the sum of the two vectors,

$$r_{k,l,\alpha}=\left|\mathbf{R}_0+\mathbf{p}_{k,l}\right|,\quad \mathbf{p}_{k,l}=\mathbf{x}x_k+\mathbf{y}y_l,\quad \mathbf{R}_0=\mathbf{x}R_0\sin\theta_\alpha+\mathbf{y}R_0\cos\theta_\alpha. \tag{3.29}$$

The circle arcs can be drawn with the nearest neighbor interpolation as,

$$c_{i,\alpha}\left(x_k, y_l\right)=\begin{cases} a_i & \text{if } \left|r_{k,l,\alpha}-R_{i,\theta_\alpha}\right|<\Delta l \\ 0 & \text{otherwise} \end{cases}, \tag{3.30}$$

The near-field SAR image can be reconstructed with the superposition of the circle arcs as,

$$S_{nf}\left(x_k, y_l\right) = \frac{1}{\zeta}\sum_{i=1}^{M}\sum_{\alpha=1}^{\zeta} c_{i,\alpha}\left(x_k, y_l\right). \tag{3.31}$$

Some scattering centers can have lower amplitude than the others. This issue may cause the loss of some scattering centers after the thresholding process (will be explained in the next subsection). Thus, imaging with the unity amplitudes $(a_i = 1)$ for all the scattering centers increases the dynamic range of the developed algorithm. Therefore, the SAR images should be reconstructed with the unity amplitudes. The estimated complex amplitude of each scattering center will be determined in the amplitude extraction process (will be explained in the next section).

3.4. Image Segmentation

Both far-field and near-field BP require discretization of the imaging window, interpolation on each pixel, and superposition process, causing non-zero pixel values on the background and artifacts around the scattering centers. These problems increase the unfavorable effects of the PSF with decreasing quality of the reconstructed image and RCS extraction accuracy. Selection of meaningful features from the reconstructed image (using the Otsu thresholding and amplitude extraction that will be explained next) helps to eliminate the corruptive impacts of the PSF, which will be shown with numerical results.

At the beginning of the segmentation process, the reconstructed image is divided by the highest pixel intensity. Thus, each pixel value in the resultant image is in the interval $[0,1]$. Due to the imaging with the unity amplitude, the pixel values around the scattering centers have closer intensity to the upper bound of the interval compared to the background components. In other words, the artifacts have lower pixel values than the unity scattering center pixels do. With this motivation, these artifacts are suppressed in this paper by processing $h(x,y) = S^2(x,y)$ that provides an increased dynamic range to the Otsu thresholding.

3.4.1. Otsu Thresholding

In this work, Otsu thresholding [27] is used for removing background from the $S(x, y)$. Otsu method assumes that the histogram of an image is composed of compacted and well separated groups which correspond to the background and scattering centers [28]. Assume a gray level image $h_g(x, y)$, which can be generated by scaling the pixel values of $h(x, y)$ to the interval $[0, I-1]$ and rounding to the nearest integer value. Here, the subscript g denotes the gray level version of $h(x, y)$, and I denotes the number of gray levels.

For the gray level image $h_g(x, y)$, the mean values of the background group and the scattering center group, respectively, are

$$\mu_1(T) = \sum_{i=0}^{T} ip(i) \Big/ \sum_{i=0}^{T} p(i),\ \mu_2(T) = \sum_{i=T+1}^{I-1} ip(i) \Big/ \sum_{i=T+1}^{I-1} p(i), \tag{3.32}$$

where T is the threshold level, $p(i)$ is the histogram of the ith gray level in $h_g(x, y)$ [28]. Variance of each group and the overall variance are

$$\sigma_1^2 = \sum_{i=0}^{T} \left(i - \mu_1(T)\right)^2 p(i) \Big/ \sum_{i=0}^{T} p(i) \tag{3.33}$$

$$\sigma_2^2 = \sum_{i=T+1}^{I-1} \left(i - \mu_2(T)\right)^2 p(i) \Big/ \sum_{i=T+1}^{I-1} p(i) \tag{3.34}$$

$$\sigma_T^2 = \sigma_1^2 \sum_{i=0}^{T} p(i) + \sigma_2^2 \sum_{i=T+1}^{I-1} p(i), \tag{3.35}$$

respectively [28]. The optimum threshold level should be found by minimizing the overall variance (3.35). The pixel values of $F(x_k, y_k)$ that satisfy $h_g(x_k, y_l) < T$ are set to the zero in order to suppress the background.

Otsu thresholding is sensitive to the amplitude differences of the scattering centers. If a scatterer has amplitude that is under the threshold value, the corresponding peak region will be lost. In order to fix this issue, instead of using extracted amplitudes, a_i, in (3.27) and (3.30), unity amplitude ($a_i = 1$) can be used in the imaging step. Henceforth, using unity amplitude will be referred as "the

normalization process." This way, the locations of the scattering centers can be determined with great resolution in expense of ignoring the scattering center amplitudes. Hence, an additional amplitude extraction process, which will be explained later, will be required.

3.4.2. Amplitude Extraction

Although Otsu's method suppresses the background components in the image, some non-zero pixels may still exist in the resultant background. This issue causes over-segmentation that decreases the RCS accuracy if all features for the non-zero pixels are used. Fortunately, this problem can be fixed by using the amplitude extraction procedure, which is formulated next.

In the far-field (or near-field) case, assume that the planar (or circular) projection of the two dimensional position of each non-zero pixel in $F(x,y)$ is $R^{\alpha}_{x''y''}$, at a look angle θ_{α}. Note that $R^{\alpha}_{x''y''}$ can be calculated by using the pixel positions of $F(x,y)$ in (3.4) (or (3.5)).

A distance vector, $\mathbf{d}_{i,\alpha}$, $i \in [1,2,\ldots,M]$, can be produced for the ith scattering center as,

$$\mathbf{d}_{i,\alpha} = \left[d_{i,\alpha}\left(x''_1, y''_1\right), d_{i,\alpha}\left(x''_2, y''_2\right), \ldots, d_{i,\alpha}\left(x''_J, y''_J\right) \right]_{1\times J} \tag{3.36}$$

$$d_{i,\alpha}\left(x''_j, y''_j\right) = \left| R_{i,\theta_{\alpha}} - R^{\alpha}_{x''_j y''_j} \right|, \tag{3.37}$$

where J is the number of non-zero pixels in $F(x,y)$. Let s be the index of the minimum element of $\mathbf{d}_i$. Then, the features for the ith scatterer should be selected as,

$$\left(x'_i, y'_i\right) = \left(x''_s, y''_s\right), \quad a'_i = a_i. \tag{3.38}$$

Note that with (3.38), both the locations and complex amplitudes of M point scatterers have been obtained. These are the estimated scattering centers that are ready to be used for the RCS extraction for the target.

3.5. Summary of the IPBP Method

In Figure 3.2, the flow chart of the developed IPBP method is summarized.

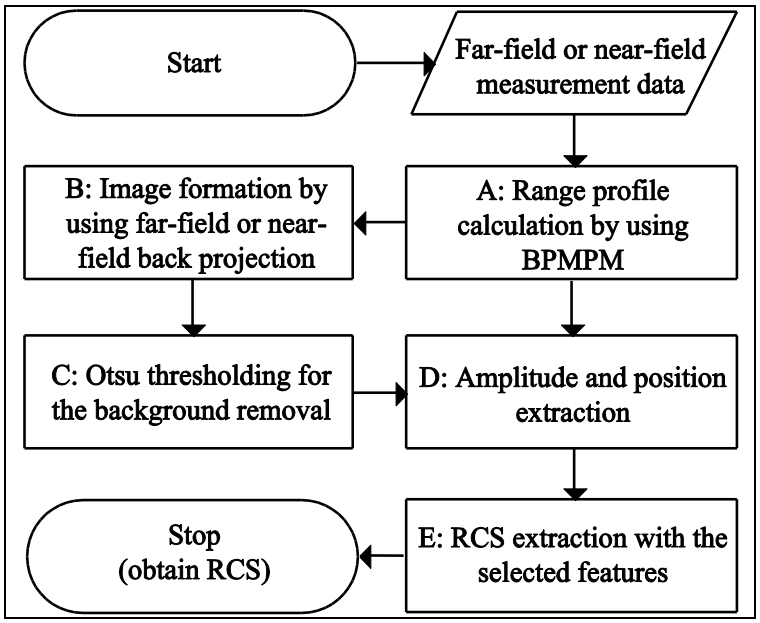

Figure 3.2: Flow chart of the IPBP method.

Firstly, BPMPM is used in order to find the range profiles with super resolution at each aspect angle (block A). Next, SAR/ISAR images are formed with an appropriate back-projection method that depends on the measurement distance and frequency. The normalization process is preferred in the image formation step (block B) in order not to lose any peak regions during the thresholding stage in block C. In order to perform feature extraction from the blurred image, the mentioned image segmentation algorithm (block C and D) is carried out. In this segmentation algorithm, firstly, the square of the formed image in block B is obtained to increase the accuracy of Otsu's thresholding. Secondly, amplitude extraction is carried out in block D to select features (position and amplitude) from the thresholded image and range profiles (calculated with the BPMPM). Although the range and cross-range positions are obtained with improved resolution as the output of block C, the amplitude of each scatterer is not valid because of the normalization process. Therefore, correct amplitude values are obtained by using the range profiles generated in Block A. Then, the obtained features for the scattering centers are used for the far-field RCS estimation at short distances.

3.6. Simulations

The performance of IPBP was examined for both far-field and near-field cases with 10 GHz center frequency, $B = 1$ GHz, and $N = 1024$. The pencil parameter $L = 512$. For comparison, the far-field SAR images, which are obtained with IFFT and BP, were reconstructed with $B = 8$ GHz that leads to $\Delta R = 18.75$ mm range resolution. The measurement distances were taken for far-field and near-field cases as $R_0 = 75$ m and 3 m, respectively. The aspect angles were taken in the interval $[-15°, 15°]$ with 30 equispaced angles. In Section 3.6.1, the pixel dimensions are chosen large enough (for producing legible figures) by defining the imaging window with 55×55 pixel resolution. In Section 3.6.2, the number of pixels is increased to 2048×2048 in order to narrow the pixel dimensions and, hence, to increase the RCS extraction accuracy. RCS versus aspect angle graphs were plotted at 10.5 GHz frequency with $0.15°$ angle step. RCS versus frequency graphs were plotted in the interval 9.5 GHz to 10.5 GHz at $0°$ aspect angle with 12.66 MHz steps. The synthetic data for the point scatterers used in both far-field and near-field simulations are given in Table 3.1.

Table 3.1: Coefficients and positions of the five point scatterers used to reconstruct far-field and near-field SAR images.

Scat. No.	Scat. Coeff. (a_i)	x-pos (x_i) [m]	y-pos (y_i) [m]
1	$0.3500 + j0.3517$	0.3407	0.1593
2	$0.0728 + j0.3077$	–0.2457	0.0472
3	$0.2511 + j0.5853$	0.3143	–0.3614
4	$0.2464 + j0.2198$	–0.2565	–0.3507
5	$0.4733 + j0.9172$	0.4293	–0.2425

3.6.1. SAR Imaging and Segmentation

In Figure 3.3, the reconstructed far-field and near-field 55×55 SAR images are given. It can be seen in Figure 3.3 a) and c) that the artifacts around the scatterers exist because of the PSF of the PBP. These artifacts are removed from the image with the developed segmentation algorithm as shown Figure 3.3 b) and d). Thus, IPBP produces better image quality than the PBP.

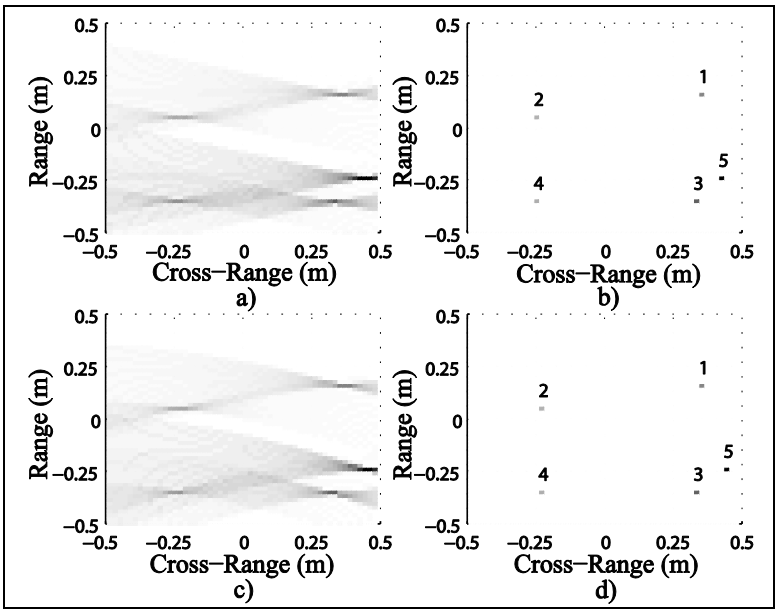

Figure 3.3: Reconstructed ISAR images for simulation data. a) Far-field PBP. b) Far-field IPBP. c) Near-field PBP. d) Near-field IPBP.

In order to show the practical usefulness of the IPBP method, the simulation times will be given. All simulations have been done in MATLAB with an Intel i7-3770 CPU. Range profiles have been obtained within 7.3 s in both of the far-field and near-field cases. Then, the images in Figure 3.3 b) and d) have been reconstructed within 0.3 s. A realistic target may have a larger linear dimension compared to our simulation scenario. In this case, the spatial extent of the imaging window must be increased until the target's geometry fits within this window. Therefore, the number of pixels must be increased in order to get the same pixel width of Figure 3.3 b) and d). In order to simulate this scenario, the imaging procedure has been performed for various pixel resolutions and spatial extents. The simulation times for the far-field (or near-field) SAR imaging can be seen from Table 3.2. Note that the range profile calculation is independent from the pixel resolution or spatial extents. Therefore, the simulation times for the range profile calculation are omitted from Table 3.2. It can be understood from the simulation times that the introduced imaging method has a complexity proportional to the total number of pixels.

As a comparison between the PBP, IPBP, and CBP, first range profiles have been obtained by using the FFT with 8 GHz bandwidth, which is eight times greater than that used by the BPMPM in this paper. Then, SAR images have been formed with these range profiles by using the MATLAB's built in function *iradon()*, which

is an implementation of the CBP for the far-field case. These images can be seen Figure 3.4.

Table 3.2: Simulation times for the image reconstruction procedure.

Pixel Resolution	Spatial Extent [m]	Simulation Time [s]
330×330	3	1.15
660×660	6	4.72
1320×1320	12	18.67
2640×2640	24	72.12

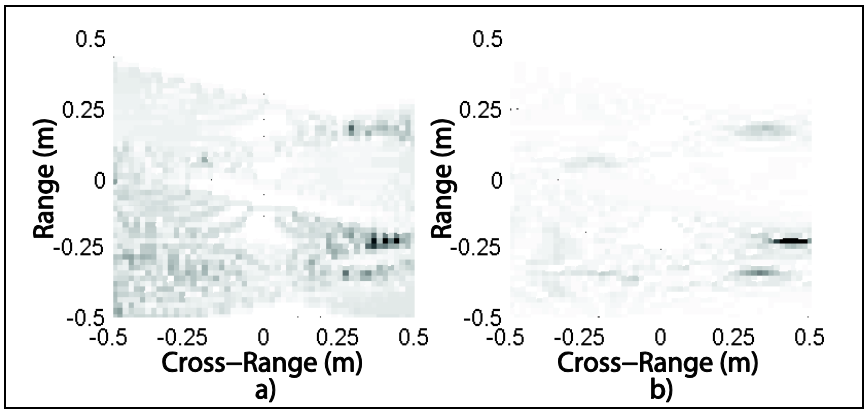

Figure 3.4: Reconstructed far-field SAR image via CBP by using the range profiles. a) With complex amplitudes. b) With absolute values of amplitudes.

Although the bandwidth is 1 GHz in the PBP and IPBP methods, Figure 3.4 has worse definition and quality than Figure 3.3 b) and d). Note that in real-life measurements, the complex reflectivity of each scattering center changes within the 8 GHz bandwidth. Thus, the difference in quality between the IPBP and the CBP (see Figure 3.3 b), d), and Figure 3.4) will be bigger than our simulations for real-life measurements in favor of the IPBP. This enhancement on the image quality leads to the increase of predicted RCS accuracy as demonstrated in Section 3.6.2.

If it is not desired to predict RCS of a target, absolute values of the complex amplitudes can be used. This yields a clearer SAR image than the obtained SAR image that is formed with the complex amplitudes as seen in Figure 3.4 a) and b). But, complex reflectivity of each scatterer is required in the RCS calculations. Note that although images in Figure 3.3 are formed with complex amplitudes, the performance of the IPBP given in Figure 3.3 b) and d) is much better than the performance of CBP depicted in Figure 3.4.

For the PBP and CBP, the cross-range resolution depends on the angular extent. Larger angular extent leads to form a SAR image with better resolution in the cross-range direction. But, the tomography-based RCS calculation should be done in a narrow angular extent because of the shadowing and the complex scattering phenomena for complex targets [3].

3.6.2. RCS Extraction

The RCS extraction was carried out by using (3.8) with meaningful features obtained by the IPBP (equation (3.38)). In Figure 3.5, "theoretical" results are obtained by using the values in Table 3.1 directly in (3.8) and both "PBP" and "IPBP" results are produced from synthetically generated data. Theory and the IPBP give quite similar RCS values at different aspect angles or frequencies. In Figure 3.5 a), the RCS error is negligible at each aspect angle with IPBP, while the RCS error can reach approximately $50\,\mathrm{dB}$ with the PBP. Similar results prevail in the near-field case as shown in Figure 3.6.

The main objective of this study is to extract the RCS values from near-field measurement data in order to alleviate far-field requirement issues. For this reason, the extracted RCS values in both far-field and near-field cases should be similar. It can be seen from a cross-comparison of Figure 3.5 and Figure 3.6 that RCS values match with each other at each aspect angle and frequency across far-field and near-field cases. These graphs indicate that reliable RCS extraction from near-field measurement data is possible if IPBP is used. Figure 3.5 and Figure 3.6 have been obtained within 70.35 s. In order to test the usefulness of the IPBP method, the image size has been increased to 8192×8192 pixels. Then the simulation time including range profile calculation, image reconstruction, and RCS extraction has been recorded as 711 s. This image size corresponds to 1.8 mm pixel width for a target having 15 m linear dimension. This pixel width is 0.064 times lower than the wavelength that corresponds to the maximum frequency.

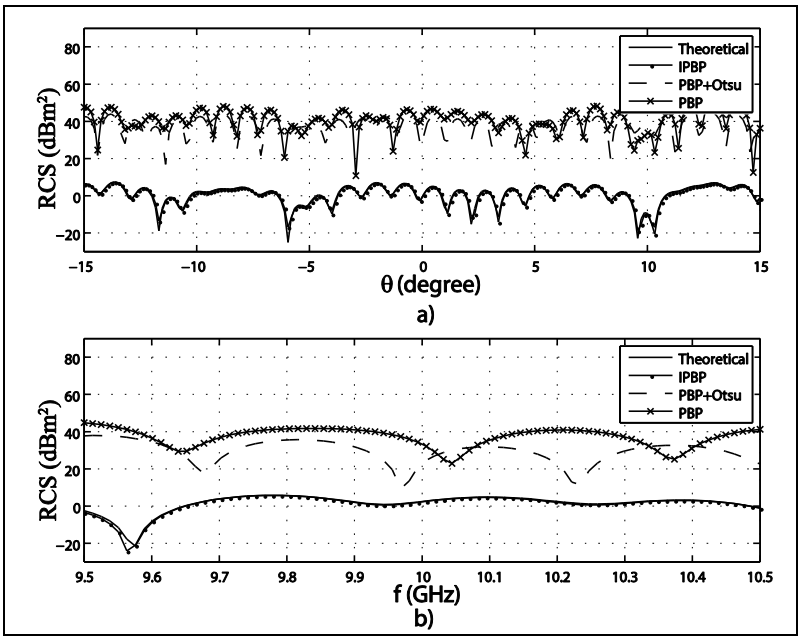

Figure 3.5: Far-field RCS extraction results. a) RCS versus aspect angle graph. b) RCS versus frequency graph.

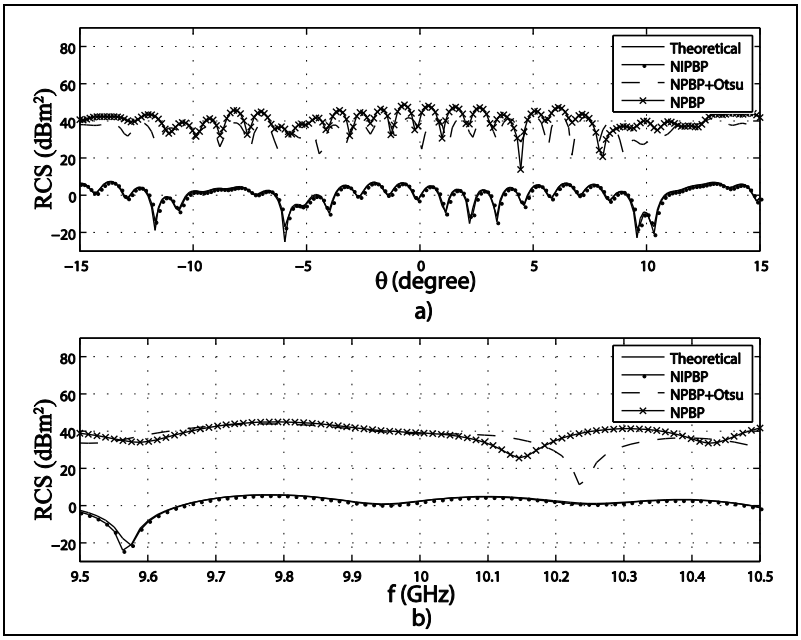

Figure 3.6: Near-field RCS extraction results. a) RCS versus aspect angle graph. b) RCS versus frequency graph.

As a further demonstration for the efficacy of employing the normalization process, results were generated without the normalization process. It is expected that some of the scatterers will be lost and the RCS errors will increase. RCS simulation results are given in Figure 3.7 and Figure 3.8 without using normalization process. Scatterers 2 and 4 (see Table 3.1) are lost without using normalization process,

causing degradation of RCS accuracy for the far-field case. But, this corruption doesn't exist with the normalization process. For the near-field case, a similar situation is experienced as demonstrated in Figure 3.8. The scatterers 1, 2 and 4 are lost if normalization process is not used. These results show the importance of normalization process.

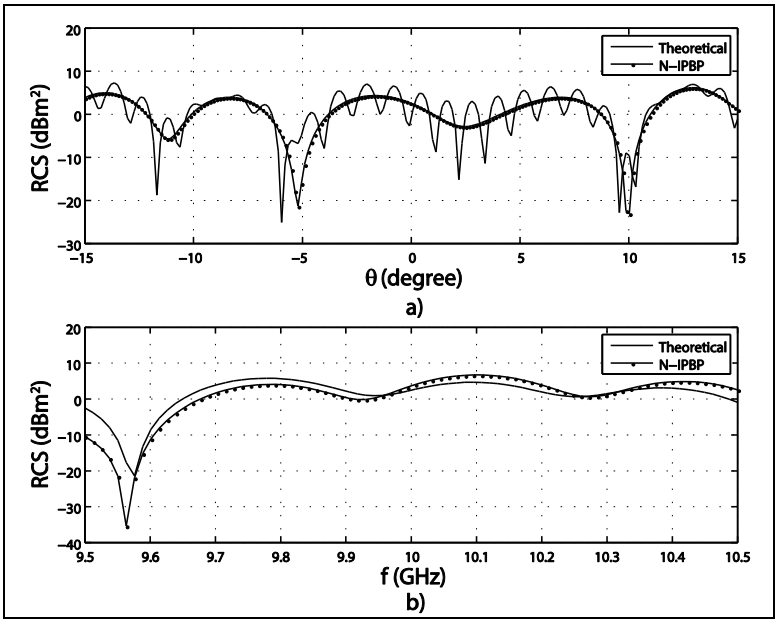

Figure 3.7: Far-field RCS extraction results by using non-normalized IPBP (N-IPBP). a) RCS versus aspect angle graph. b) RCS versus frequency graph.

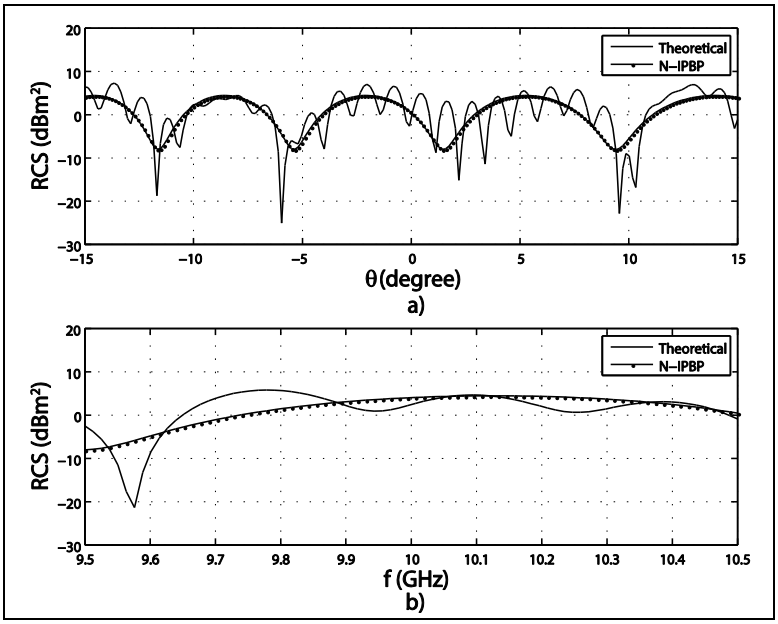

Figure 3.8: Near-field RCS extraction results by N-IPBP. a) RCS versus aspect angle graph. b) RCS versus frequency graph.

3.7. Measurements

In this work, not only synthetic data were used, but also two real targets were considered in order to test the accuracy of the IPBP method. The first target is composed of a $30\,\text{cm}$ and a $50\,\text{cm}$ trihedral reflectors. The second target is a ship model that is composed of dihedral, cube and cylinder reflectors. Measurements were done to measure the S parameters of these targets in the Open Range Electromagnetic Laboratory (ASEMLAB; Açık Saha Elektromanyetik Laboratuarı), which has spotlight mode inverse SAR (ISAR) setup.

Target-1 is shown in Figure 3.9. The stationary antenna collects received echo signals from the rotating target with θ_0 denoting the look angle. Target alignment is done such a way that when $\theta_0 = 0°$, the line that connects the corner reflectors makes an angle of approximately $45°$ with the down range direction. Measurements were done at $10\,\text{GHz}$ center frequency. The largest linear dimension of this target is $1.8\,\text{m}$. It means that the far-field requirement for this target is approximately $216\,\text{m}$. Thus, the measurements were done at $R_0 = 308.3\,\text{m}$ and $R_0 = 133.1\,\text{m}$ for the far-field and near-field cases, respectively. The number of frequency points was selected as $N = 6401$ that requires the maximum bandwidth 1.5524 GHz (and $3.5814\,\text{GHz}$) for the far-field (and near-field cases) to guarantee proper unambiguous range. Based on this, measurements were done with $B = 1\,\text{GHz}$ ($B = 2\,\text{GHz}$) bandwidth, which lead to the $R_{\max} = 480\,\text{m}$ ($R_{\max} = 240\,\text{m}$) maximum measurable distances in the far-field (near-field) case. The measurement angles were in the range $[-15°, 15°]$ with $0.5°$ angle step.

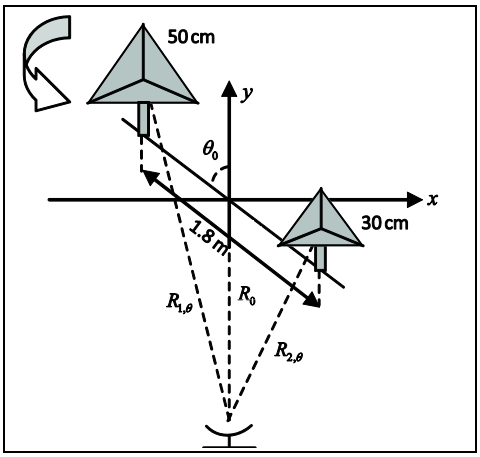

Figure 3.9: Target-1.

The main purpose of the use of trihedral corner reflectors is that each of these reflectors has one scattering center with the well-known RCS value,

$$\sigma_{\max}(\lambda) = 10\log_{10}(4\pi l^4/(3\lambda^2)), \tag{3.39}$$

where l is the length of each perpendicular side of the trihedral [29], [30]. Thus, the theoretical number of scattering centers is known as *a priori* as 2 in the measurements of the target in Figure 3.9. The 50 cm trihedral has 24.637 dBm^2 RCS value, which is 15.763 dBm^2 for the 30 cm trihedral.

Target-2 is shown in Figure 3.10. Each reflector (cylinder, cube, dihedral) residing on the ship's geometry has some scattering centers, which are apart from each other with a distance not bigger than the measurement wavelength. In this respect, this target is useful to test the limits of the IPBP.

The shadowing effect is extremely important for the tomography-based RCS extraction for complex targets. This effect can't be tested with target-1. However, the reflectors residing on target-2 geometry shadow each other at different aspect angles. For example, the cube is shadowed by the dihedral reflector near the zero degree aspect angle.

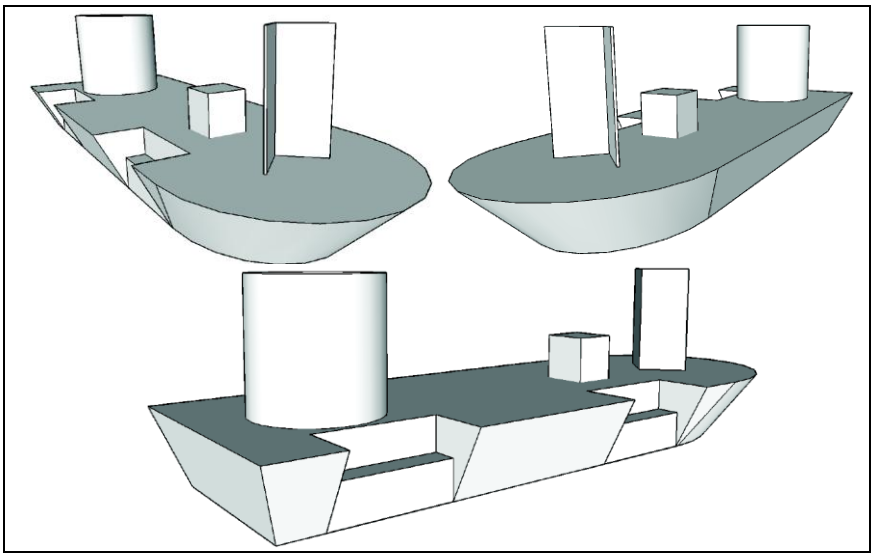

Figure 3.10: Target-2.

The dimensions of target-2 are given in Figure 3.11. This target has a maximum linear dimension of 1.5 m. Thus, the far-field requirement for this target is

satisfied at 150 m at 10 GHz. Therefore, the far-field and near-field measurements are done at the measurement distances of 300 m and 49 m, respectively. All measurements are done with 1 GHz bandwidth. The number of points is selected as 6401 and 1601 for the far-field and near-field cases, respectively. Target-2 is rotated $360°$ with $0.5°$ step size in the interval $[-180°, 180°]$. The aspect angle along the prow of the ship is marked as 0°. This target is rotated around its center point.

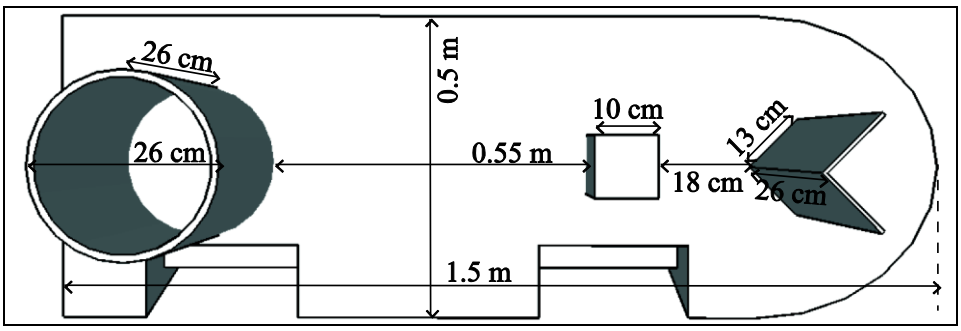

Figure 3.11: Target-2 dimensions.

In order to calibrate measurement setup, a 50 cm trihedral was used as a reference target. Total loss of the system is calculated by using the formula,

$$\sigma_{\text{loss}} = \sigma_{\text{reference}} - \sigma_{\text{measured}}. \tag{3.40}$$

Then, the calibration is performed by summing the total system loss to the extracted RCS values [21] $\sigma = \sigma_{\text{loss}} + \sigma_{\text{extracted}}$.

3.7.1. Range Profile Calculation with BPMPM

The collected open range measurement data are composed of the back-scattered EM waves from the targets in Figure 3.9 and Figure 3.10, as well as the clutter that is caused by other scatterers in the range. A gating process with an appropriate windowing function enhances the performance of MPM. In this study, Bartlett-Hann window of order 200 was used. For target-1, the maximum cut-off ranges are 310 m and 135 m in the far-field and near-field cases, respectively. The corresponding minimum cut-off ranges are 306 m and 131 m. The maximum cut-off ranges are selected for target-2 as 302 m and 49.5 m in the far-field and near-field

cases, respectively. The corresponding minimum cut-off ranges are 300 m and 47.5 m. The group delay of the preferred FIR filter was 100 samples.

The BPMPM converges to the Cramer-Rao bound with a Signal-to-Noise Ratio (SNR) greater than 25 dB [26]. Therefore, 25 dB SNR value is required for proper imaging and RCS extraction with IPBP. In order to satisfy this requirement, the incoming signals are averaged with a factor Q, increasing the SNR value by $10\log_{10}(Q)$ [19]. For target-1, Q is taken as 64 in the network analyzer. It was seen during the measurements that target-2 has lower reflected signal power than target-1. Thus, in order to increase the SNR, the Q is selected for target-2 as 180 and 256 for the far-field and near-field measurements, respectively. The obtained range profiles are given in Figure 3.12. It can be seen from this image that at the 0° aspect angle for target-1, the 1 GHz bandwidth is enough to distinguish two reflectors in the IFFT results. But, at the aspect angle -89° for target-2, this bandwidth is not sufficient in the IFFT results to distinguish the dihedral and cube reflectors. However, BPMPM gives the range values of the scattering centers on these dihedral and cube reflectors with super resolution. The reason is that the range resolution of BPMPM is not bounded directly by the bandwidth. This is one of the advantages of the BPMPM over the IFFT.

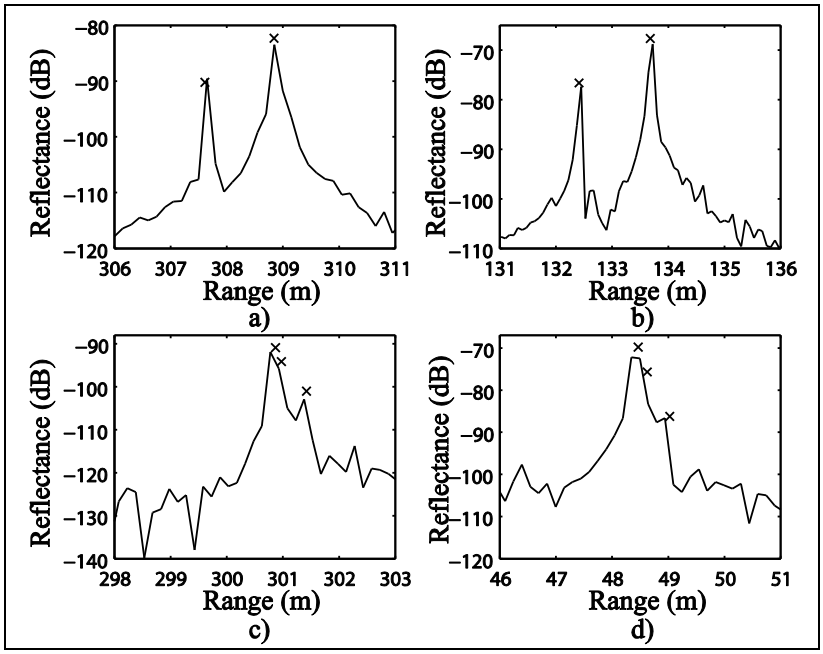

Figure 3.12: Calculated range profiles, -- denotes IFFT, x marker denotes BPMPM. a) Far-field result at 0° for target-1. b) Near-field result at 0° for target-1. c) Far-field result at -89° for target-2. d) Near-field result at -89° for target-2.

3.7.2. ISAR Imaging and Segmentation

Figure 3.13 shows that the far-field and near-field ISAR images are quite similar to each other when IPBP is applied to target-1 measurement data. This figure is a clue that the extracted RCS values will be similar for the far-field and near-field cases as shown in the next section. In addition to this, IPBP method has a super resolution in both range and cross-range dimensions, while PBP and NPBP have artifacts in the cross-range dimension.

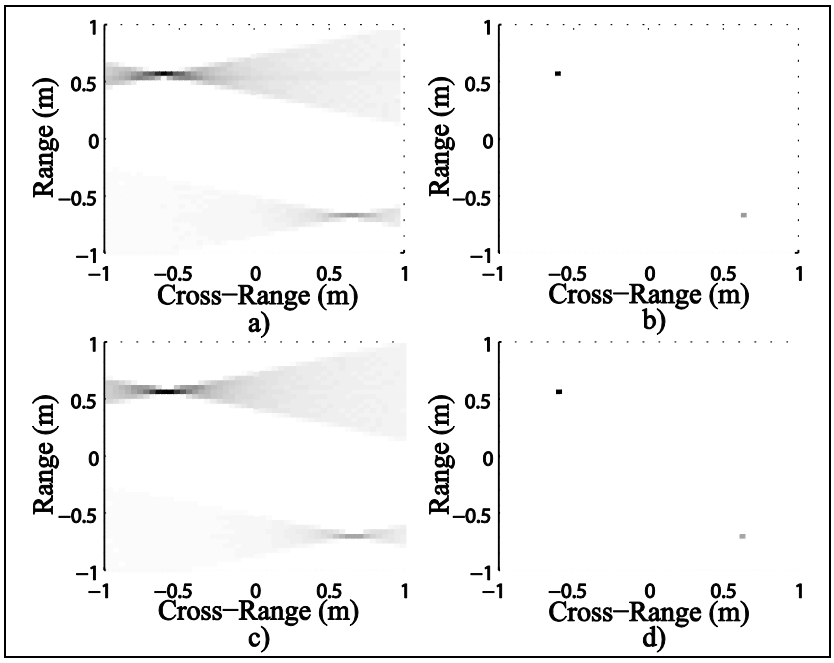

Figure 3.13: Reconstructed ISAR images for target-1. a) Far-field PBP. b) Far-field IPBP. c) Near-field PBP. d) Near-field IPBP.

At the beginning of the measurements for target-2, the dimensions of the target were measured. It was noted that the center of the dihedral is located at $(x = 0, y = -0.45)$ meters. The cube and cylinders are residing on target-2 with the centers $(x = 0, y = -0.23)$ and $(x = 0, y = 0.5)$ meters. It is expected that the highly reflective regions on target-2 are the dihedral, cube, and cylinder reflectors. The IPBP ISAR images for target-2 support this expectation as depicted in Figure 3.14. Besides, the centers and dimensions of the highly reflective regions on the image are similar to the real values.

In order to emphasize the super resolution of the IPBP, CBP and IPBP results are compared by using the same bandwidth (1 GHz) that yields a range resolution of

15 cm for the CBP. The CBP images are shown in Figure 3.15 for the far-field case. Figure 3.15 a) has been reconstructed with the original data. In order to produce a legible image, the measured signals have been up-sampled by 2 yielding half the pixel size of that used in Figure 3.15 a). This modified image is shown in Figure 3.15 b).

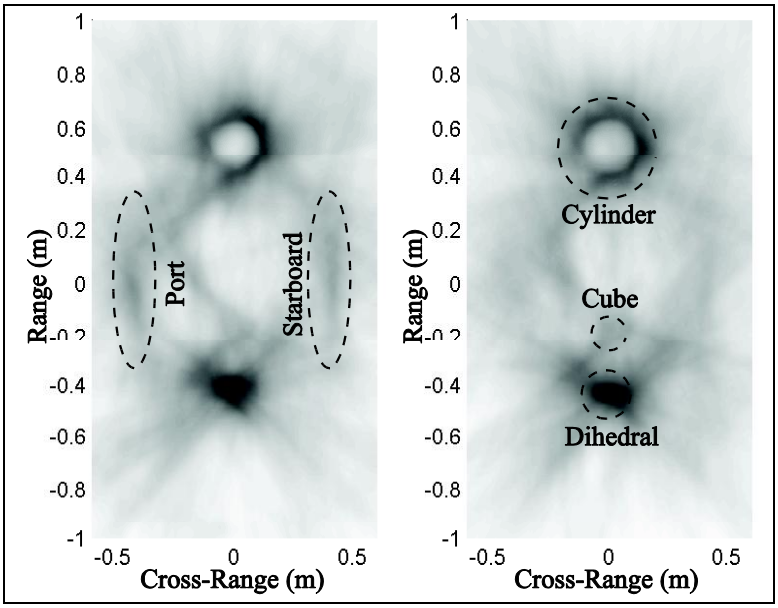

Figure 3.14: IPBP ISAR images for target-2 with real measurements. The left one is in the far-field. The right one is in the near-field.

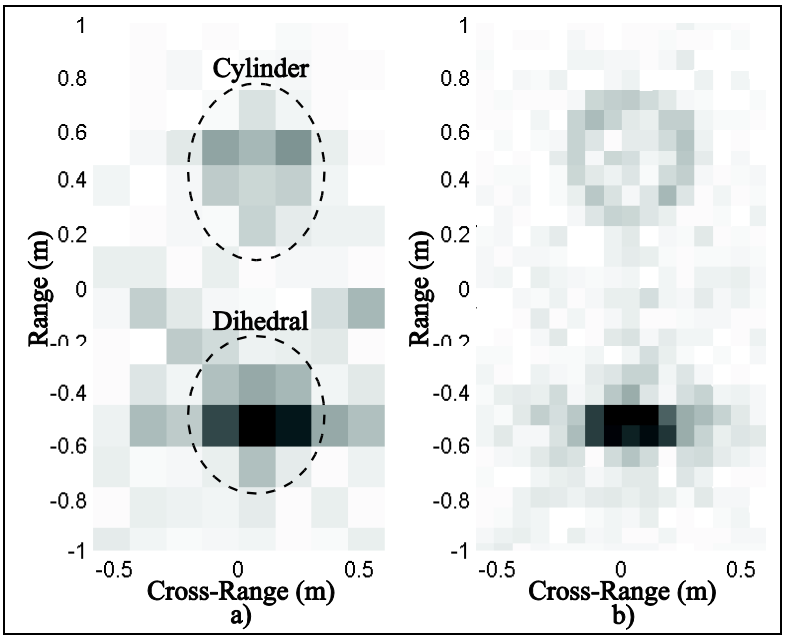

Figure 3.15: Far-field CBP ISAR image for target-2. a) Original image. b) Reconstructed image with up-sampled data.

According to Figure 3.15, a 15 cm range resolution (1 GHz bandwidth) is not sufficient to reconstruct the reflectors in the image. For example, the cylinder has a diameter of 26 cm. The pixel width of Figure 3.15 a) is equal to the range resolution (15 cm) that is almost the same with the radii of the cylinder. As another example, the dihedral has an edge length of 12.5 cm, which is lower than the range resolution of the CBP. Thus, the dihedral can't be reconstructed efficiently because of the poor resolution of the CBP. Data up-sampling does not affect main lobe widths of the point spread function of the CBP in the range and cross-range dimensions because these main lobe widths are dependent on the bandwidth and angular extent. Therefore, the resolution problems shown in Figure 3.15 a) still exist in the modified image as seen in Figure 3.15 b). However, the IPBP has much better resolution than the CBP as shown in Figure 3.14 and Figure 3.15.

3.7.3. RCS Extraction

The extracted RCS values for target-1 are shown in Figure 3.16. The far-field and near-field RCS values match with each other, while there is a small angular shift (less than $0.08°$) between the far-field and near-field results at $12°$ and larger angles. The reason of this shift is attributed to the environmental effects on the target such as wind, which had different strengths during the measurement times.

In [3], it is said that the extracted scattering center model at a particular angle is not valid for over a large angular extent, depending on the target complexity and reconstruction accuracy. It is demonstrated in [3] that the reconstructed range profile from scattering center model at $0°$ matches with the actual range profile at $-5°$ if SBR is used. In the far-field case, RCS at a particular angle is the Fourier transform of the range profile in the same line of sight. The similarity between range profiles from the reconstructed scattering center model and actual range profiles supports the gist of the algorithms used here for RCS extraction with high accuracy. Thus, in the case of RCS extraction from SAR/ISAR images, reconstruction should be repeated at multiple windows in the angular dimension in order to increase the extraction accuracy. Figure 3.16 shows that the extracted far-field and near-field RCS values match with each other in a $30°$ angular range, which is 6 times greater than the demonstrated angular extent in [3]. This result is obtained from the simple target-1.

A more challenging test for the validation of the IPBP was done with target-2 in terms of RCS extraction. The extracted RCS values are given in Figure 3.17 and Figure 3.18.

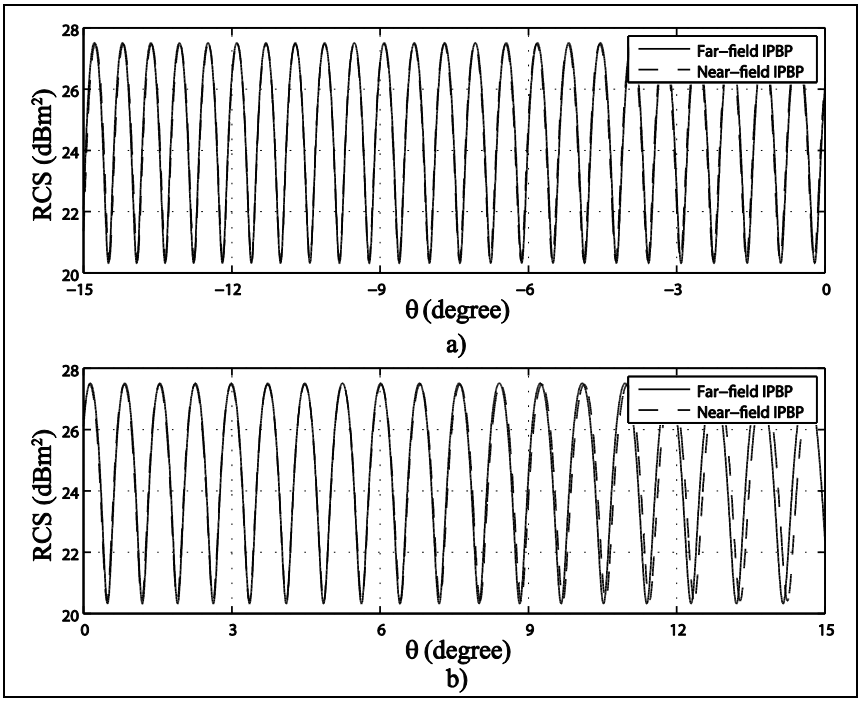

Figure 3.16: Extracted RCS values at 10 GHz frequency. a) $\theta \in [-15°, 0]$. b) $\theta \in [0, 15°]$.

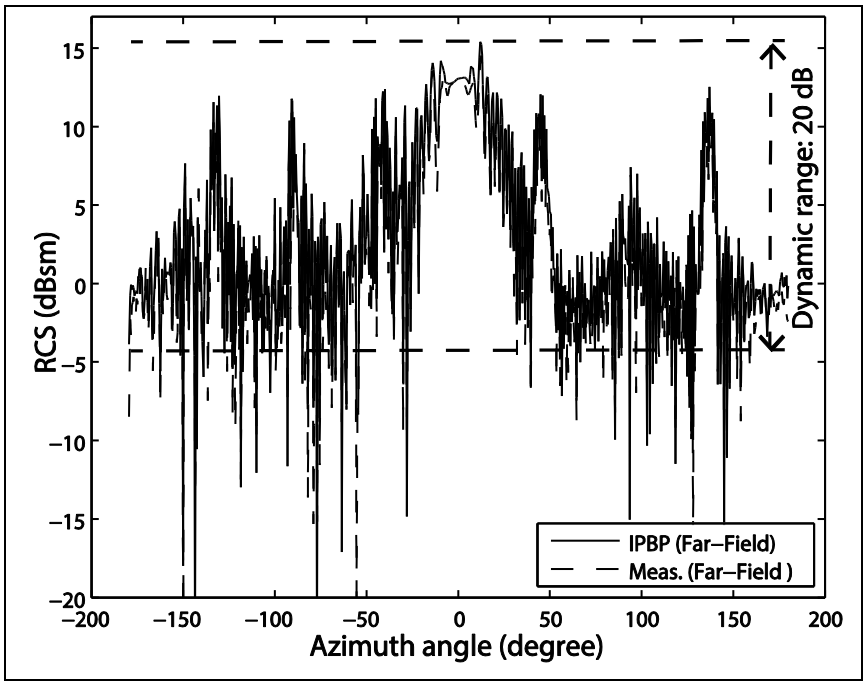

Figure 3.17: Extracted RCS values for target-2 with far-field measurements.

In order to eliminate any doubt about representing a complex target with the point reflectivity model given in (3.2), the extracted point scattering centers in the far-field case were used to reconstruct the RCS values. Figure 3.17 consists of two RCS curves. The first one is the reconstructed RCS values from the extracted point scattering centers. The second one is the directly measured RCS values, which don't contain any post-processing because the far-field criteria is already satisfied during the measurements. As it can be seen from Figure 3.17, the reconstructed and measured RCS values match with each other within a dynamic range of 20 dB. The arithmetic mean of the error between these two RCS curves is 1.17 dBsm within this dynamic range. This error becomes smaller as the dynamic range is reduced.

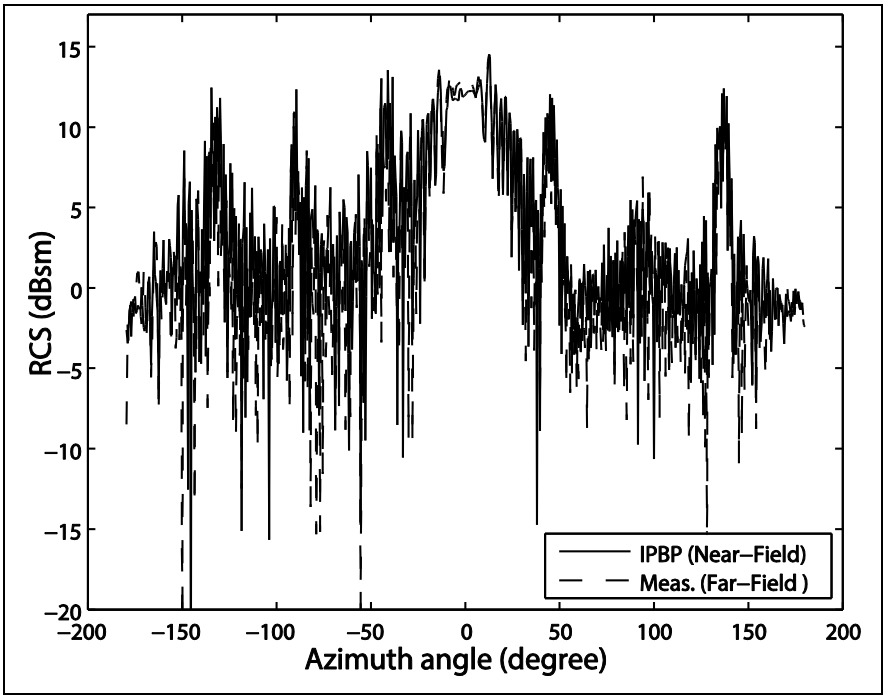

Figure 3.18: Extracted RCS values for target-2 with near-field measurements.

After making sure that the assumed point reflectivity model is valid for complex targets, the extracted scattering centers with near-field measurements were used to estimate the RCS values of target-2. The estimated and measured RCS values are given in Figure 3.18. The arithmetic mean of the error between the measured and estimated RCS curves is 2.46 dBsm. Again, this error becomes smaller as the dynamic range decreases.

In spite of high accuracy in the IPBP results, the efficacy of this method is restricted by some physical reasons. SAR/ISAR measurements in an indoor

laboratory may need large hangar dimensions especially for huge targets. Besides, rotating a target such as a ship or tank to different aspect angles with a pedestal/pylon system is very difficult (often not possible). Therefore, performing measurements in their operational environment becomes crucial. In this thesis, another algorithm, which leads to extraction of scattering centers in target's operational environment, is developed and introduced in the next chapter. This is an important facility to setup measurement systems.

4. HIGH RESOLUTION CHIRP ISAR IMAGING WITH NEAR-FIELD MEASUREMENTS

Performing measurements in a real operational environment reduces the physical difficulties significantly. But, these type of measurements for moving objects require fast sweep time not to face with a timing/synchronization problem. For the computation of range profiles, there are several types of signaling techniques, of which performance is closely dependent to the timing issues [19]. Using the single frequency pulse signals yields poor range resolution that depends on the pulse width [19]. SFCW signals have better range resolution than the single frequency pulse signals [19]. But, it leads to an increase in the computational burden and timing problems for some non-stationary targets. For the stepped-frequency pulse (SFP) signals, the range resolution and unambiguous range depend on the bandwidth and number of frequency points, respectively. In order to complete the frequency sweep, more than one pulse are needed [19]. Thus, another trade-off between the range resolution and measurement time still exists in SFCW signaling. In order to avoid this trade-off, chirp signals have been widely used. The frequency bandwidth is scanned within only one pulse with a modulation index in the chirp signals [19]. Thus, it is possible to get high range resolution via chirp signals by consuming much lower measurement time than that needed by SFCW or SFP.

In this thesis, a new Chirp imaging method, which simultaneously overcomes the problems related with the range resolution, measurement time and far-field requirement, is presented. To this end, range profiles are estimated by applying the MPM to Chirp signals for the first time in the literature. This decreases the required time for the frequency sweep and lead to get high range resolution with a reasonable pulse width. The introduced method allows to compute range profiles with much better range resolution than the traditional chirp signal processing.

The developed IPBP method in this thesis (see Chapter 3) is designed for the circular rotation of object with a constant measurement distance. Therefore, IPBP is not suitable for imaging of an moving object. In this thesis, another high resolution imaging method is introduced for the extraction of scattering centers of moving objects in a near-field range. This method has super resolution in both range and cross-range dimensions likewise the IPBP method.

4.1. Formulation of the Signal Model

The assumed ISAR imaging geometry is illustrated in Figure 4.1.

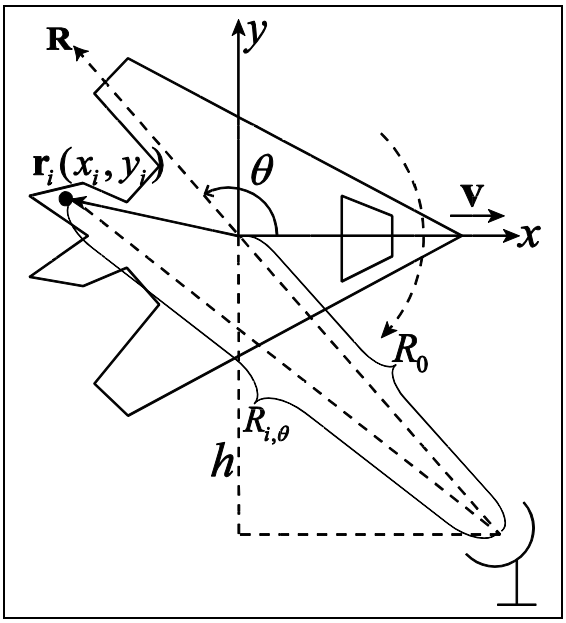

Figure 4.1: Chirp ISAR measurement setup.

In this geometry, two different monostatic measurement setups, which are referred to as "Case-I" and "Case-II" in the rest of this paper, are depicted. In Case-I, the target revolves around the center of the coordinate system with a distance R_0 from the antenna. In Case-II, the target moves along the x direction with a velocity $\mathbf{v}$ at a constant height h. Generally, Case-I is preferred to measure the EM response of a target in a laboratory. But, it is difficult to work with realistic objects in a laboratory environment because of physical restrictions. For these applications, it can be useful to measure the EM response of a target in its operational environment by preferring the Case-II geometry. In both of these setups, the aspect angle is referred to as θ and the line of sight (range) vector is $\mathbf{R}$. The position of the ith scattering center is represented with a distance vector $\mathbf{r}_i$ or (x_i, y_i).

In this algorithm, the point scattering center model given in (3.2) is used. The transmitted chirp signal has the form,

$$s_t(t) = \exp\left(j2\pi \left(f_c t + \frac{1}{2}\alpha t^2 \right) \right) \quad ; \quad 0 \le t \le T_p, \tag{4.1}$$

where f_c is the start frequency, t is time variable varying within the pulse width T_p, and α is the chirp rate [31]. The bandwidth B is equal to αT_p. In Case-II, the non-stationary target generates a frequency shift in the incoming signals. For a constant measurement frequency, f_o, the Doppler shift can be written as $f_D = 2f_o v_r/c$, where v_r is the radial velocity of the target and c is the speed of light [32]. In this article, it is assumed that $v_r \ll c$, $f_D \ll f_c$ and thus the Doppler effect is neglected. The reflected signal from the ith scattering center is [31],

$$s_{i,\theta}(t) = \frac{a_i}{R_{i,\theta}^2} \exp\left(j2\pi \left(f_c(t-\tau_{i,\theta}) + \frac{1}{2}\alpha(t-\tau_{i,\theta})^2 \right) \right), \tag{4.2}$$

where, $\tau_{i,\theta} = 2R_{i,\theta}/c$ is the time delay, caused by the round-trip time. In order to reduce the sampling rate, the received and transmitted signals are mixed in the receiver. Then the generated IF signal is [31],

$$s_{i,\theta}^{IF}(t) = \frac{a_i}{R_{i,\theta}^2} \exp\left(j2\pi \left(f_c\tau_{i,\theta} + \alpha t\tau_{i,\theta} - \frac{1}{2}\alpha\tau_{i,\theta}^2 \right) \right). \tag{4.3}$$

Eqn. (4.3) can be also written as,

$$s_{i,\theta}^{IF}(t) = A_{i,\theta} \exp\left(j2\pi\alpha t\tau_{i,\theta} \right), \tag{4.4}$$

$$A_{i,\theta} = \frac{a_i}{R_{i,\theta}^2} \exp\left(j2\pi \left(f_c\tau_{i,\theta} - \frac{1}{2}\alpha\tau_{i,\theta}^2 \right) \right). \tag{4.5}$$

According to the target's point reflectivity model, reflected signals from the M scattering centers are added together in the receiver. Thus, eqn. (4.2) becomes,

$$s_\theta(t) = \left(\sum_{i=1}^{M} s_{i,\theta}(t) \right) + s_C(t) + n_o(t), \tag{4.6}$$

where $s_c(t)$ corresponds to the clutter and $n_o(t)$ is the noise components. In order to decrease the noise power, the incoming signals are averaged as,

$$s_\theta(t) = \frac{1}{Q}\sum_{q=1}^{Q}\left(\left(\sum_{i=1}^{M} s_{i,\theta}(t)\right) + s_C(t) + n_{o,q}(t)\right), \tag{4.7}$$

$$s_\theta(t) = \left(\sum_{i=1}^{M} s_{i,\theta}(t)\right) + s_C(t) + \underbrace{\frac{1}{Q}\sum_{q=1}^{Q} n_{o,q}(t)}_{n_o'(t)}, \tag{4.8}$$

where, Q is the number of averaging, $n_o'(t)$ is the suppressed noise signal. This procedure has the integration-improvement factor $10\log_{10}(Q)$ for the ideal predetection [19]. After this stage, the generated IF signal has the form,

$$s_\theta^{IF}(t) = \left(\sum_{i=1}^{M} A_{i,\theta}\exp\left(j2\pi\alpha t\tau_{i,\theta}\right)\right) + s_C(t) + n_o'(t). \tag{4.9}$$

In this work, the time gating is used in order to filter clutter from the received signal. The pulse generator in the receiver has a pulse repetition period T_r. Therefore, the echoes with a round-trip time $\tau_C < T_r$ are not collected by the receiver. Only the echoes that satisfy,

$$T_r \le \tau \le T_r + T_p', \quad T_p' \ge T_p + T_D, \tag{4.10}$$

is received by the radar. Here, T_p' is the pulse width of the pulse generator in the receiver, T_D is a round-trip time that corresponds to the temporal extent of the target in the down range direction. If the maximum extent of target is D, time gating can be done by setting up the pulse generator in the receiver with the cut-off timings as,

$$T_r^{\text{cutt}} = 2R_{\min}/c, T_p^{\text{cutt}} = T_p + 2D/c. \tag{4.11}$$

Here, $R_{\min}$ corresponds to the starting point of the gating process. After this stage, eqn. (4.9) becomes,

$$g_\theta^{IF}(t) = \sum_{i=1}^{M} A_{i,\theta}\exp\left(j2\pi\alpha t\tau_{i,\theta}\right) + \underbrace{s_C'(t) + n_o'(t)}_{\eta'(t)}, \tag{4.12}$$

where $g_\theta^{IF}(t)$ is the time gated IF signal, $s_C'(t)$ corresponds to the remaining clutter in the IF signal. The Fourier transform of eqn. (4.12) is [22],

$$G_\theta^{IF}(\tau) = \sum_{i=1}^{M} A_{i,\theta}\delta\left(\tau - \alpha\tau_{i,\theta}\right) + FT\left\{\eta'(t)\right\}. \tag{4.13}$$

Here, $FT(\cdot)$ is the Fourier transform operator. Eqn. (4.13) can be computed via the fast Fourier transform (FFT) as,

$$\hat{G}_\theta^{IF}(\tau) = FFT\left\{g_\theta^{IF}(t)\right\}, \tag{4.14}$$

with a round-trip time resolution $\Delta\tau = 1/\alpha T_p = 1/B$. Then, the range profiles are obtained as $\hat{G}_\theta^{IF}(c\tau/2)$ with a range resolution $\Delta R = (c\Delta\tau)/2 = c/(2B)$ [2]. This resolution causes complex amplitude and position errors due to the limited bandwidth.

4.2. Matrix Pencil Method for Chirp Signals

Sampling of the signal given in eqn. (4.12) yields

$$\Gamma_n = g_\theta^{IF}\left(n\Delta t\right) = \sum_{i=1}^{M} A_{i,\theta} z_{i,\theta}^{n} + \eta'(n\Delta t), \quad n = 0,1,\ldots,N-1 \tag{4.15}$$

$$z_{i,\theta} = \exp(j2\pi\alpha\tau_{i,\theta}\Delta t), \tag{4.16}$$

where N is the number of time points and Δt is the sampling step size. In the rest of the formulations, $\eta'(n\Delta t)$ is omitted for simplicity. But, in the numerical simulations, $\eta'(n\Delta t)$ are added to the incoming signals with different SNR values. In order to reduce the sampling rate, the time-gated IF signal is multiplied with $\exp\left(-j2\pi\alpha t\tau_0\right)$ yielding,

$$\tilde{g}_\theta^{IF}(t) = \sum_{i=1}^{M} A_{i,\theta}\exp\left(j2\pi\alpha t\tilde{\tau}_{i,\theta}\right), \tag{4.17}$$

where $\tau_0 = 2R_0/c$, $\tilde{\tau}_{i,\theta} = \tau_{i,\theta} - \tau_0$. Eqn. (4.17) can be written as,

$$F_n = \tilde{g}_\theta^{IF}\left(n\Delta t\right) = \sum_{i=1}^{M} A_{i,\theta}\tilde{z}_{i,\theta}^{n}, \quad \tilde{z}_{i,\theta} = \exp(j2\pi\alpha\tilde{\tau}_{i,\theta}\Delta t). \tag{4.18}$$

The MPM gives $A_{i,\theta}$, and $\tilde{z}_{i,\theta}$, with super resolution from the band limited data [24], if $D < 1/(\alpha\Delta t)$ is satisfied. Assume the Hankel matrix of F_n as (3.14), the poles of eqn. (4.18) can be estimated with the same eigenvalue calculation explained in the IPBP method [24], [33]. The range value of the ith scattering center can be estimated as,

$$\tau'_{i,\theta} = \frac{\angle\tilde{z}'_{i,\theta}}{2\pi\alpha\Delta t} + \tau_0, \;\; R'_{i,\theta} = \frac{c\tau'_{i,\theta}}{2}, \;\; i = 1, 2, \ldots, M, \tag{4.19}$$

Once the poles have been extracted, (4.18) can be inverted as,

$$\left[A'_{1,\theta}, A'_{2,\theta}, \ldots, A'_{M,\theta}\right]^T = \left(\left[\mathbf{Z}\right]^T\right)^{\dagger}\left[F_0, F_1, \ldots, F_{N-1}\right]^T, \tag{4.20}$$

in order to estimate $A_{i,\theta}$. Here, $\left[\mathbf{Z}\right]$ is the same matrix given in (3.20) while consisting of estimated poles $\tilde{z}'_{i,\theta}$. Then, using eqn. (4.5), the complex amplitude of the ith scattering center can be estimated as,

$$a'_i = A'_{i,\theta}\left(R'_{i,\theta}\right)^2 \exp\left(-j2\pi\left(f_c\tau'_{i,\theta} - \frac{1}{2}\alpha\left(\tau'_{i,\theta}\right)^2\right)\right). \tag{4.21}$$

4.3. ISAR Image Reconstruction

Assume that $S(x, y)$—which is akin to the $f(x, y)$—has X and Y grids with Δx and Δy resolutions in the x and y directions, respectively. The image has the dimensions,

$$N_x = 1 + D_x/\Delta x, \quad N_y = 1 + D_y/\Delta y, \tag{4.22}$$

where D_x and D_y are the extents of the image. The kth element of the imaging grids has the coordinates,

$$x_k = -\frac{D_x}{2} + (k-1)\Delta x, \;\; y_l = -\frac{D_y}{2} + (l-1)\Delta y, \tag{4.23}$$

$$k = 1, 2, \ldots, N_x; \;\; l = 1, 2, \ldots, N_y. \tag{4.24}$$

The circular projection of the pixel positions x and y to the line of sight is,

$$\mathrm{T}_{klm} = \sqrt{R_0^2(m) + p_{kl}^2 + 2R_0(m)(x_k \cos\theta(m) + y_l \sin\theta(m))}, \tag{4.25}$$

where $p_{kl}^2 = x_k^2 + y_l^2$, m is the angular sampling index, which takes the values of $m = 1, 2\ldots, \gamma$, γ is the number of aspect angles. Note that for the moving object, R_0 varies with the aspect angles as,

$$R_0(m) = h/\sin(\pi - \theta(m)), \tag{4.26}$$

in Case-II. The ith scattering center can be found by the Minimum Square Error (MSE) definition as,

$$e_i(k,l) = \frac{1}{\gamma}\sum_{m=1}^{\gamma}\left|\mathrm{T}_{klm} - R_{i,\theta(m)}\right|^2, \tag{4.27}$$

$$\left(k_{0i}, l_{0i}\right) = \arg\min_{k,l}\left[e_i(k,l)\right], \quad \left(x_i', y_i'\right) = \left(x_\xi, y_\psi\right), \tag{4.28}$$

where $\xi = k_{0i}$, $\psi = l_{0i}$, x_i' and y_i' are the estimated x and y values of the ith scattering center. The corresponding pixel value is $S\left(x_i', y_i'\right) = a_i'$. This procedure is repeated for all of the scattering centers in order to estimate $f(x,y)$. Note that in order to use Case-II, θ can be determined with the estimation of the direction of arrival (DOA) by using [32], [34], [35].

4.4. Simulations

In this section, the performance of the developed algorithm is examined. The start frequency is chosen as $f_c = 10$ GHz and the bandwidth is $B = 600$ MHz. In

order to emphasize the contribution of this study, the given scattering center features in [13] are used. These features can be seen in Table 4.1.

Table 4.1: Coefficients and positions of the six point scattering centers used to reconstruct near-field ISAR images.

Scat. No.	Scat. Coeff. (a_i)	x-pos (x_i) [m]	y-pos (y_i) [m]
1	$0.767\exp(j0)$	2	2
2	$0.494\exp(j\pi/4)$	4	–4
3	$1.000\exp(j\pi/2)$	–6	–6
4	$0.634\exp(j3\pi/4)$	–8	8
5	$0.442\exp(j\pi)$	10	10
6	$0.765\exp(j5\pi/4)$	12	–12

The largest linear distance between these scattering centers is $D = 28.3$ m. Thus, the far-field requirement for these scattering centers is $R_o \geq 2D^2(f_c + B)/c =$ 56.5 km. In order to generate near-field data, the measurement distance is taken as $R_o = 100$ m for "Case-I" (see Figure 4.1). For "Case-II", it is assumed that the target moves along the x direction with a constant height $h = 400$ m. The aspect angles are $\theta = [90, 91, 92, 93]$ degrees that yield a $3°$ angular extent, which is the same value used for the PBP in [13]. This selection for the angular extent allows to compare the cross-range resolution of the developed algorithm with the IPBP and CBP.

The pulse width in the transmitter is chosen as $T_p = 200$ ns. In order to process the time gating, The pulse width in the receiver is taken as $T_p^{\text{cutt}} = 389$ ns, which yields 28.35 m gating range that is 5 cm larger than D. The number of time points are choosen as 4000, that yields $L = 2000$. In "Case-I", the pulse repetition period is taken as $T_r^{\text{cutt}} = 866.7$ ns. In "Case-II", this value is taken as $T_r^{\text{cutt}} = 2\,(R_o(m) - D)/c$. The ISAR images are formed by using uniform grids with the resolutions $\Delta x = \Delta y = 3$ cm and the number of pixels $N_x = N_y = 1000$. White Gaussian noise is added to data with the SNR values $[5, 10, 15, 20]$ in dB. The number of averaging is taken as $Q = 128$. In order to demonstrate the superiority of the MPM over FFT, range profiles are graphed for Case-I and Case-II with 5 dB SNR value at $\theta = 90°$. The performance of the developed algorithm is depicted in Figure 4.2, Figure 4.3, and Figure 4.4.

The range profiles in Figure 4.2 show that FFT suffers from poor range resolution, $\Delta R = c/(2B)$, that causes amplitude and range errors. But, the MPM gives the scattering center features with super resolution, which doesn't directly depend on bandwidth unlike the traditional chirp SAR. In order to show the resolution of MPM, two point targets having unity amplitude and range values 50 m and 50.15 m are considered with 5 dB SNR. The range profiles of these targets are given in Figure 4.3. For the FFT based chirp SAR/ISAR, 600 MHz bandwidth yields 25 cm range resolution. The point targets in Figure 4.3 having 15 cm range difference between each other. Thus, the FFT based method suffers from poor range resolution as given in Figure 4.3. But, the developed algorithm using the MPM gives the scattering center features with super resolution. The estimated amplitudes and positions are $A' = [0.9949, 0.9959]$ and $R' = [50.1518, 50.0002]$.

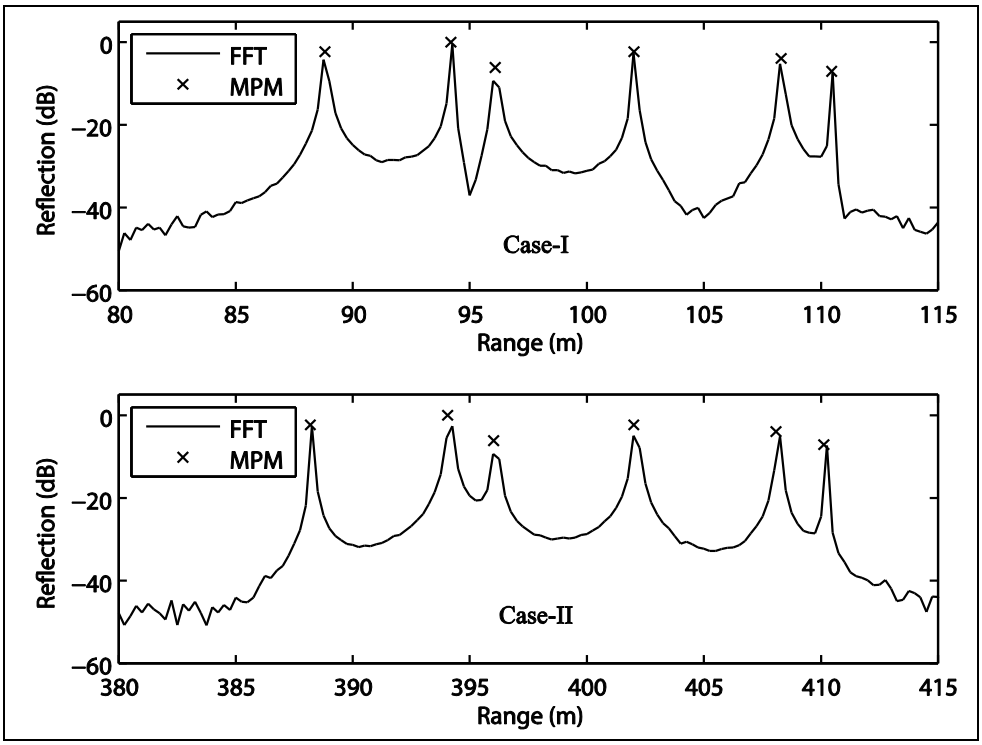

Figure 4.2: Calculated range profiles via FFT and MPM with 5 dB SNR value at aspect angle $\theta = 90°$.

After the range profile calculation, the imaging is done for the point targets in Table 4.1. The results can be seen in Figure 4.4. The developed algorithm gives one pixel width scattering centers with various SNR values, while PBP has poor resolution in the cross-range dimension as depicted in Figure 3 in [13].

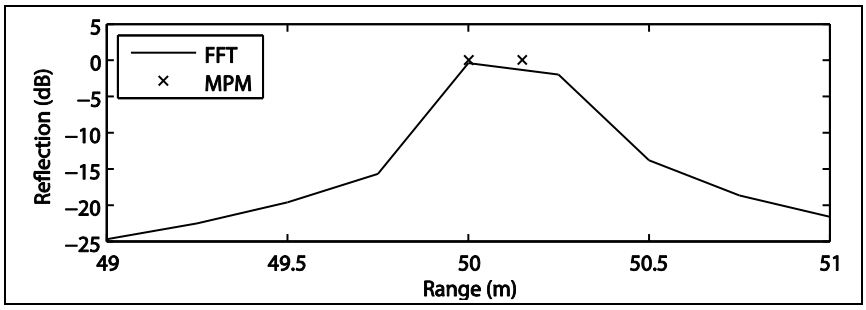

Figure 4.3: A comparison between the range resolution of FFT and MPM.

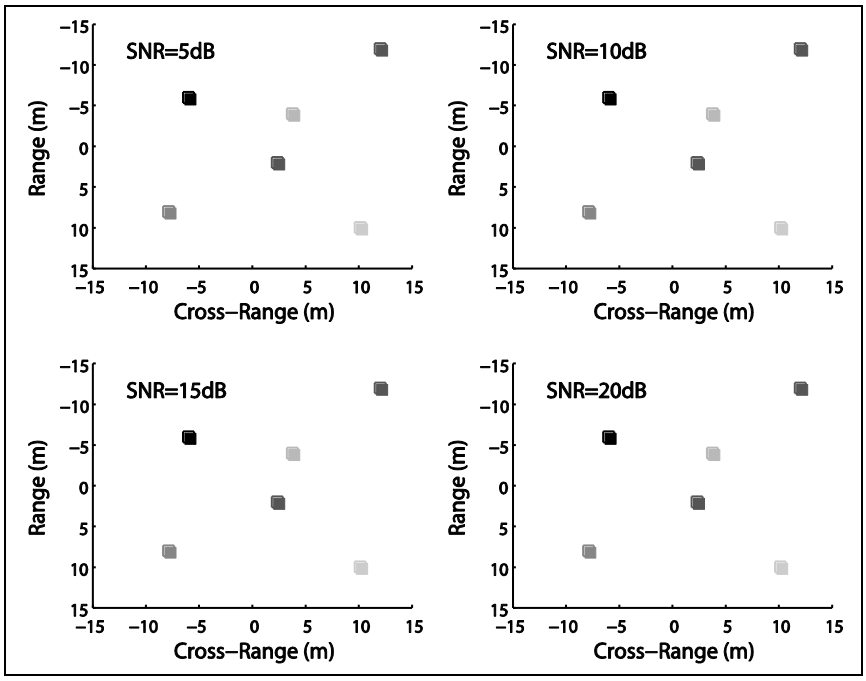

Figure 4.4: Reconstructed ISAR images with the developed Chirp ISAR imaging algorithm for “Case-I and II”.

As another comparison, the multiplicative noise ratio (MNR) defined in [13],

$$\mathrm{MNR} = 10\log_{10}\frac{\sum(\text{pixels outside "mainlobe"})^2}{\sum(\text{pixels inside "mainlobe"})^2}, \tag{4.29}$$

is considered. The “main-lobe” is set to be a 5×5 pixel square centered at the peak as represented in [13]. The ISAR images have a rectangular grid, that is composed of 64×64 number of pixels as in [13]. A point scattering center at the position $(x, y) = (-23, 24)$ in pixel units is considered. The angular extent is taken as the same value in [13] as $3°$. The results show that while the MNR value for the

developed algorithm is $-\infty$, it is written in [13] that MNR values for the PBP and CBP are -18.9 and -30.5, respectively. This means that for the developed algorithm, there are no pixels outside the "main-lobe" due to the high resolution.

As another example, two point scattering centers having unity amplitude and the positions $(x_1, y_1) = (0, 0)$ and $(x_2, y_2) = (0.3, -0.3)$ are used with 64×64 imaging size and 2.5 cm pixel width in rectangular shape. It can be seen from Figure 4.5 that the developed algorithm yields one pixel width estimated scattering centers. But, PBP and CBP suffers from artifacts as depicted in Figure 6 in [13].

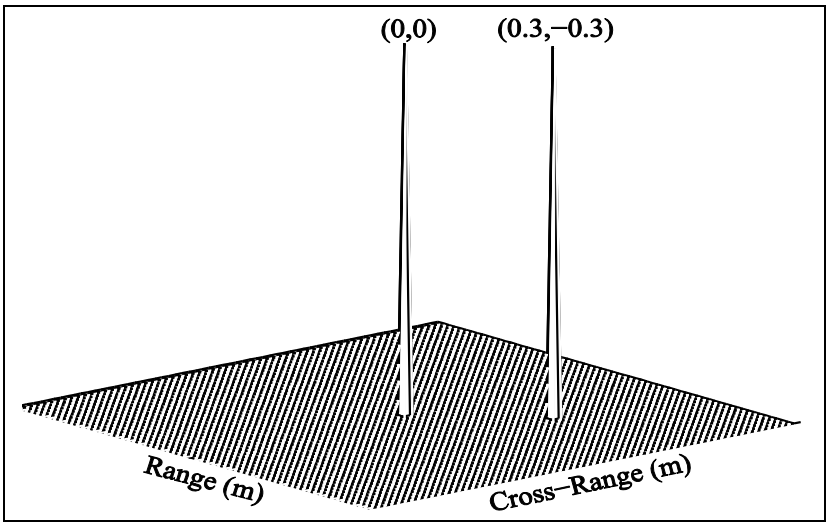

Figure 4.5: Results of the developed algorithm in "Case-I and II" for the point targets located at $(0, 0)$ and $(0.3, -0.3)$.

The point spread function of the PBP is dependent on the measurement frequency and the angular extent as given in eqn. (44) in [13]. This function tends to the Dirac-Delta function by increasing the angular extent. But, the point scattering center model used in this algorithm and [13] is not valid for complex targets in large angular extents [3]. The developed algorithm in this paper doesn't require a large angular extent for high resolution imaging. Moreover, the developed algorithm is valid for near-field measurements. But, PBP needs the far-field requirement [13].

To give the required SNR value of the developed method, ISAR images are reconstructed with the SNR value 0 dB. The results are given in Figure 4.6. It can be seen from Table 4.1 and Figure 4.6 that some scattering centers have wrong positions with 0 dB SNR value. The results given in this section is generated with $Q = 128$, improves the SNR value by $10\log_{10}(128) = 21.07$ dB.

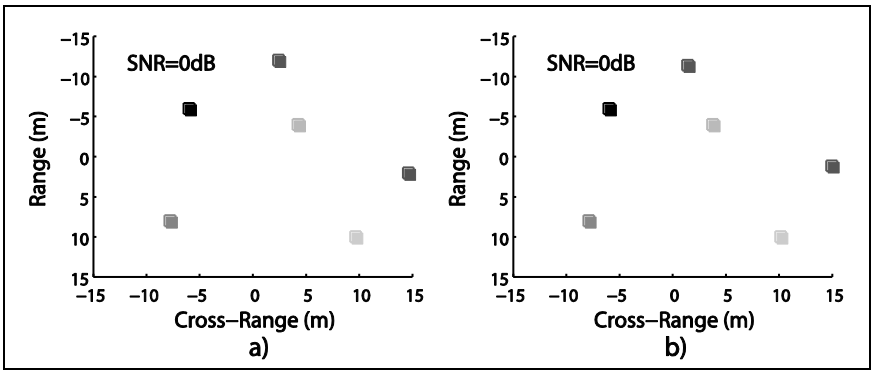

Figure 4.6: Reconstructed ISAR images with the SNR value 0 dB. a) “Case-I”. b) “Case-II”.

The introduced method in Section-IIC uses the MPM. It can be seen in [26] that the performance of the MPM tends to the Cramer-Rao bound with a SNR value greater than 26 dB. Thus, the required SNR value for the developed algorithm is,

$$\mathrm{SNR}_r = 26 - 10\log_{10}(Q), \tag{4.30}$$

in dB. For $Q = 128$, it is expected that the developed algorithm gives high accuracy with a SNR value greater than $\mathrm{SNR}_r = 26 - 10\log_{10}(128) = 4.93$ dB. The reconstructed ISAR images in Figure 4.4 and Figure 4.6 support this expectation.

Although this algorithm gives accurate results while neglecting the Doppler effect in simulation data, it restricts the efficacy of algorithm due to the arbitrary radial velocity in real life applications. It can be said that this algorithm is suitable for slowly moving targets such as a ship on sea. A faster target, for instance a plane or helicopter, can’t be measured by using this algorithm due to the not negligible radial velocity. In this case, a range distortion named as range-Doppler coupling occurs in the range profiles. Hence, the extracted scattering centers may not have reliable features. In order to alleviate this restriction and extract the RCS values, another algorithm is developed and introduced in the next section.

5. ESTIMATING RADAR CROSS SECTION OF MOVING TARGETS WITH NEAR-FIELD MEASUREMENTS

In this chapter, a new method, which is an improved version of the previous algorithm (see Chapter 4), is presented to determine the RCS of moving targets. This method has two novel approaches. First, Doppler frequencies (and radial velocities) are calculated with super-resolution that is not bounded by the pulse width or frequency bandwidth. This yields better accuracy compared to the FFT-based techniques. High resolution Doppler frequency estimation brings another novel approach for compensating the range-Doppler coupling. Thus, the limitations of [17] related to the target velocity is alleviated by this algorithm. After the compensation, range profiles and ISAR images are obtained with high resolution by applying the introduced procedures in [17] to the compensated signal. Then, the extracted scattering centers are used for the RCS determination with near-field measurements. It is another novelty in this work that the introduced approach does not need the far-field requirement or a laboratory environment for RCS calculations. Such that RCS values are determined in the operational environment of moving targets.

5.1. Formulation of the Problem

The ISAR imaging geometry in this chapter is very similar with the previous one (see Chapter 4). The main difference is that the target moves along an arbitrary direction $\vec{e}_d$ with a radial velocity $\mathbf{v}$, while this vector represents a direction in the horizontal plane in Chapter 4.

In this algorithm, the same point scattering center model $f(x,y)$ given in eqn. (3.2) is used. The round-trip time corresponding to the ith scattering center can be expressed as [36], [37], where, ν is the modulus of the radial velocity [36].

$$\tau_{i,\theta}(t) = \alpha_i + \beta t, \quad \alpha_i = 2R_{i,\theta}/c, \quad \beta = 2\nu/c. \tag{5.1}$$

Then, putting $\tau_{i,\theta}(t)$ into the IF signal $s_{i,\theta}^{IF}(t) = s_t(t) \times s_{i,\theta}(t)^*$ yields the following equations [36], [37]. Here, $()^*$ is the complex conjugation.

$$s_{i,\theta}^{IF}(t) = \frac{a_i^*}{R_{i,\theta}^2} \exp\left(j\left(\phi_0[i] + \phi_1[i]t + \phi_2[i]t^2\right)\right) = b_i \exp\left(j\left(\phi_1[i]t + \phi_2 t^2\right)\right), \quad (5.2)$$

$$\phi_0[i] = 2\pi f_c \alpha_i - \pi\mu\alpha_i^2,\ \phi_1[i] = 2\pi f_c \beta + 2\pi\mu\alpha_i(1-\beta),\ \phi_2 = 2\pi\mu\beta(1-0.5\beta). \quad (5.3)$$

Here, ϕ_1 and ϕ_2 can be also written as the following forms,

$$\phi_1[i] = 2\pi \underbrace{f_c\, 2v/c}_{-f_d} + 2\pi \underbrace{\mu(1-2v/c)\, 2R_{i,\theta}/c}_{\psi_i},\ \phi_2 = 4\pi\mu(1-v/c)\, v/c, \quad (5.4)$$

where f_d is the Doppler frequency caused by the radial velocity of the moving target [32]. It can be seen from eqn. (5.4) that taking FFT of eqn. (5.2) causes a range-Doppler coupling that leads to a range distortion as illustrated in [36]. Therefore, the phase terms in eqn. (5.2) related to the radial velocity should be compensated. Therefore, it is useful to estimate the Doppler frequency with a good accuracy. A high resolution technique for this estimation will be given later (see Range Profile Calculation with MPM).

After the determination of Doppler frequency and radial velocity, the range-Doppler coupling can be compensated by the multiplication [37],

$$z_{i,\theta}^{IF}(t) = s_{i,\theta}^{IF}(t) \times \exp\left(j2\pi f_d' t - j4\pi\mu(1-v'/c)\, v'/c)\, t^2\right) \cong b_i \exp\left(j2\pi\psi_i t\right), \quad (5.5)$$

where, the estimated values $f_d' \cong f_d$ and $v' \cong v$. Taking the Fourier transform of eqn. (5.5) yields,

$$z_{i,\theta}^{IF}(t) \xrightarrow{FFT} Z_{i,\theta}^{IF}(\psi) = b_i \delta(\psi - \psi_i), \quad \psi_i = 2\mu(1-2v/c)\, R_{i,\theta}/c. \quad (5.6)$$

Then the range value of the ith scattering center can be calculated as [37],

$$R_{i,\theta} = c\psi_i / (2\mu(1-2v'/c)). \quad (5.7)$$

According to the point reflectivity model, incoming signals from the M scattering centers are added together in the receiver. However, the received signal

has also clutters and noise components as explained in Chapter 4. In order to suppress the clutters and noise signals, the same time-gating and averaging procedures in Chapter 4 are also performed in this chapter.

After the summation of eqn. (5.6) over all scattering centers, the right hand side of the resultant equation can be computed via FFT with a $\psi-$resolution $\Delta\psi = 1/T_p$. Therefore, the calculated range profiles have a range resolution [37],

$$\Delta R = c\,/(2\mu T_p(1-2v'/c)) = c/(2B(1-2v'/c)), \tag{5.8}$$

Note that for a stationary target, the range resolution becomes $\Delta R = c/(2B)$ that is the traditional range resolution of such radar systems [19].

Assume that the estimated amplitudes and range values b_i' and $R_{i,\theta}'$, respectively. Then the reflectivity of each scattering center can be obtained as [37],

$$a_i' = \left(R_{i,\theta}'^2 b_i'\right)^* \exp(j\phi_0). \tag{5.9}$$

Ones these features are calculated, an ISAR image can be reconstructed via the given method in [17]. Then, putting the obtained scattering centers into eqn. (3.8) gives the estimated far-field RCS values.

5.2. Range Profile Calculation with MPM

In the previous section, it has been shown that the range-Doppler coupling should be compensated to enhance the range profile calculation accuracy. With this aim, a single frequency pulse signal is transmitted to the moving target before the Chirp signal. Therefore, it is referred to “leading signal” in the rest of this paper. This type of signaling yields a signal pocket shown in Figure 5.1. The boldface graph corresponds to the leading signal. The other one is the Chirp signal [37].

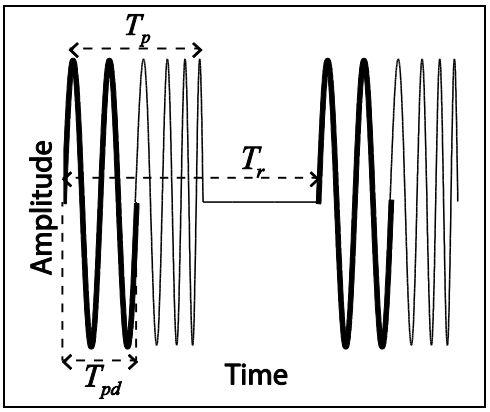

Figure 5.1: The transmitted signal pocket.

The incoming leading signal has the form,

$$l(t) = \sum_{i=1}^{M} \frac{a_i}{R_i^2} \exp(j2\pi f_c (t - \tau_i)) + \eta'(t), \tag{5.10}$$

where $0 \le t \le T_{pd}$ and $\eta'(t)$ is the noise signal. Then, the IF signal $l^{IF}(t)$ can be obtained as,

$$l^{IF}(t) = \exp(j2\pi f_c t) \times l^*(t), \tag{5.11}$$

$$l^{IF}(t) = \sum_{i=1}^{M} \frac{a_i^*}{R_i^2} \exp(j \underbrace{2\pi f_c \tau_i}_{\phi}) + \eta''(t), \;\; \phi = 4\pi f_c R_i / c + 4\pi f_c v t / c. \tag{5.12}$$

Then, the Doppler frequency is,

$$f_d = -\partial\phi(t)/2\pi\partial t = -2 f_c v / c. \tag{5.13}$$

Putting it into (5.12) yields,

$$l^{IF}(t) = C \exp(-j2\pi f_d t) + \eta''(t), \;\; C = \sum_{i=1}^{M} \frac{a_i^*}{R_i^2} \exp(j\, 4\pi f_c R_i / c). \tag{5.14}$$

The Doppler frequency and radial velocity can be estimated by performing the MPM to the sampled form of eqn. (5.14). That is [37],

$$f_d' = -\frac{\angle p'}{2\pi\Delta t},\ v' = -\frac{c f_d'}{2 f_c},\ p' = eig\left(\left[\mathbf{F}_1'\right]^{\dagger}\left[\mathbf{F}_2'\right]\right), \tag{5.15}$$

where $\left[\mathbf{F}_1'\right]$ and $\left[\mathbf{F}_2'\right]$ are the matrices obtained from the truncated Hankel matrix for the sampled form of eqn. (5.14). That is,

$$\left[\mathbf{F}_1'\right] = \left[\mathbf{f}_0'\,\mathbf{f}_1' \cdots \mathbf{f}_{L-1}'\right],\quad \left[\mathbf{F}_2'\right] = \left[\mathbf{f}_1'\,\mathbf{f}_2' \cdots \mathbf{f}_L'\right]. \tag{5.16}$$

Here, $\mathbf{f}_n'$ is the columns of the truncated Hankel matrix $\left[\mathbf{F}'\right]$ that is computed via the SVD process. Although the leading signal yields a super Doppler resolution, this signal suffers from poor range resolution. Because, the range resolution is limited by the pulse width of the leading signal. Instead of calculating range profiles with a leading signal, a Chirp signal is transmitted to the moving object with a time variable $t' = t - T_{pd}$ (see Figure 5.1). This new time variable satisfies $0 \le t' \le T_p - T_{pd}$. The de-ramped and sampled IF signal has the form,

$$s_\theta^{IF}(n'\Delta t) = \sum_{i=1}^{M} b_i \exp\left(j\left(\phi_1[i]n'\Delta t + \phi_2(n'\Delta t)^2\right)\right). \tag{5.17}$$

Here n' satisfies $t' = n'\Delta t, n' = 0,1,\ldots,N-1$. Putting the estimated Doppler frequency and radial velocity into the discrete form of eqn. (5.5) leads to [37],

$$z_\theta^{IF}(n'\Delta t) = \exp\left(j2\pi f_d' n'\Delta t - j4\pi\mu(1 - v'/c)v'/c)(n'\Delta t)^2\right) \times \sum_{i=1}^{M} s_{i,\theta}^{IF}(n'\Delta t), \tag{5.18}$$

$$z_\theta^{IF}(n'\Delta t) = \sum_{i=1}^{M} b_i \exp\left(j2\pi\psi_i n'\Delta t\right). \tag{5.19}$$

Eqn. (5.19) may need large number of samples to satisfy the Nyquist criteria $1/\Delta t \ge 2\psi_i$ if target moves at a large distance. In order not to face this problem, eqn. (5.19) should be multiplied by another exponential as [37],

$$\begin{aligned} z_\theta^{IF}(n'\Delta t) &= \exp\left(-j2\pi\psi_0 n'\Delta t\right) \times \sum_{i=1}^{M} b_i \exp\left(j2\pi\psi_i n'\Delta t\right) \\ &= \sum_{i=1}^{M} b_i \exp\left(j2\pi(\psi_i - \psi_0)n'\Delta t\right), \end{aligned} \tag{5.20}$$

$$\psi_0 = 2\mu(1-2v/c)\,R_0/c. \tag{5.21}$$

Then, the range profiles are obtained with a super resolution by performing the MPM procedure to eqn. (5.20). Then, the range value and complex amplitude of each scattering center can be calculated as [37],

$$R_{i,\theta} = R_0 + c\psi_i'/(2\mu(1-2v'/c)),\ \ \psi_i' = eig\left(\left[\mathbf{F}_1'\right]^{\dagger}\left[\mathbf{F}_2'\right]\right), \tag{5.22}$$

$$a_i' = \left(R_{i,\theta}'^2 b_i'\right)^{*}\exp\left(j2\pi f_c\alpha_i' - j\pi\mu\alpha_i'^2\right),\ \ \alpha_i' = 2R_{i,\theta}'/c, \tag{5.23}$$

$$b_i' = \left(\left[\boldsymbol{\psi}\right]^T\right)^{\dagger}\left[z_\theta^{IF}(0), z_\theta^{IF}(\Delta t),\ldots, z_\theta^{IF}((N-1)\Delta t)\right]^T, \tag{5.24}$$

where $\left[\boldsymbol{\psi}\right]$ is the Vandermonde matrix (see (3.20)), that is formed with the obtained poles ψ_i' in eqn. (5.22).

MPM facilitates a super resolution for both the Doppler frequency and range values. However, the signal-to-noise ratio (SNR) of the IF signals (for leading and Chirp signals) should be greater than 26 dB in order to reach the Cramer-Rao bound [26]. Therefore, a proper range-gating and averaging process become important to get reliable results with the MPM. The noise level of the IF signals should satisfy the condition $\mathrm{SNR}_{\mathrm{IF}} > 26 - 10\log_{10}(Q)$ [17], [37].

5.3. ISAR Image Reconstruction

In this chapter, the similar imaging technique given in Chapter 4 is used for the scattering center extraction from range profiles. The details of this technique can be found in the previous chapter (Section 4.3.). In this stage, a further process is performed in order to optimize the position of each scattering center to reduce the RCS error.

Eqn. (4.27) tends to the zero near the scattering center point (x_i, y_i). Thus, the roots of this equation gives the two dimensional position of each scattering center. This is a non-linear optimization problem that can be solved by using the Levenberg-Marquardt algorithm (LMA). The details and implementation of LMA can be found in [38]-[41]. The implementation of LMA requires an initial position vector to begin the iterations. In this section, these initial points are determined by performing the

imaging method given in [17]. Once the LMA procedure is complete, the point scattering center function is estimated with the scattering center features, a_i', x_i', y_i'.

5.4. Simulations

The performance of the developed algorithm is tested with some simulations in this section. In order to point out the contribution of this paper, the given scattering center features, a_i, x_i, y_i, in [17] are used. The simulation parameters are chosen as follows.

- $f_c = 10$ GHz, $B = 600$ MHz, $h = 4$ km, $v = 554$ km/h, $N = 1024$, $Q = 180$
- $\Delta t = 50$ ps, $T_{pd} = T_p/2 = 51.15$ ns, $\theta = [90°, 91°, 92°, 93°]$, $D_x = D_y = 30$ m
- $N_x = N_y = 2048$, $\text{SNR} = [0, 5, 10, 15]$ dB.

The RCS graphs have been drawn at 512 equispaced aspect angles. Note that the largest linear length between these scattering centers is $D = 28.3$ m. Thus, the far-field requirement for these scattering centers is $R_0 > 2D^2(f_c + B)/c = 56.5$ km. The altitude of the target is $h = 4$ km leading to a maximum measurement distance $R_{0,\max} = 4.0055$ km. Therefore, the target stays in the near-field zone for all aspect angles. In order to increase the received signal power, an amplifier has been assumed to be used in the transmitter that has 40 dB gain. In addition, the received signal has been assumed to be amplified with a low noise amplifier having 30 dB gain. Thus, the system gain is totally 70 dB.

The received signal has been gated by a pulse generator in the receiver having a pulse width $T_p^{\text{cutt}} = 302.3$ ns and the pulse repetition periods $T_r^{\text{cutt}} = 2(R_0(m) - D)/c$. These cutt-off timings yield 30 m gating range in each aspect angle.

In order to generate synthetic data, the simulation parameters have been used for the synthetic data generation. Then, the Doppler frequency and radial velocity have been determined in each aspect angle. While $\text{SNR} = 15$ dB and $\theta = 93°$, the MPM yields Doppler frequency and radial velocity errors as 0.0196 Hz and 2.9381×10^{-4} m/s, respectively. These values have been calculated as 58.9769 Hz and 0.8847 m/s by the FFT-based estimation. It is clear that the MPM-based Doppler estimation has better accuracy than the FFT-based estimation [37]. The efficacy of

the introduced compensation algorithm for the range-Doppler coupling can be seen in Figure 5.2. As it is seen from this figure, the radial velocity of the target distorts the range profiles [37]. The introduced compensation algorithm recovers the original range profile from the distorted one, efficiently. It is shown that the obtained range values (by MPM) are closely similar to the real ranges.

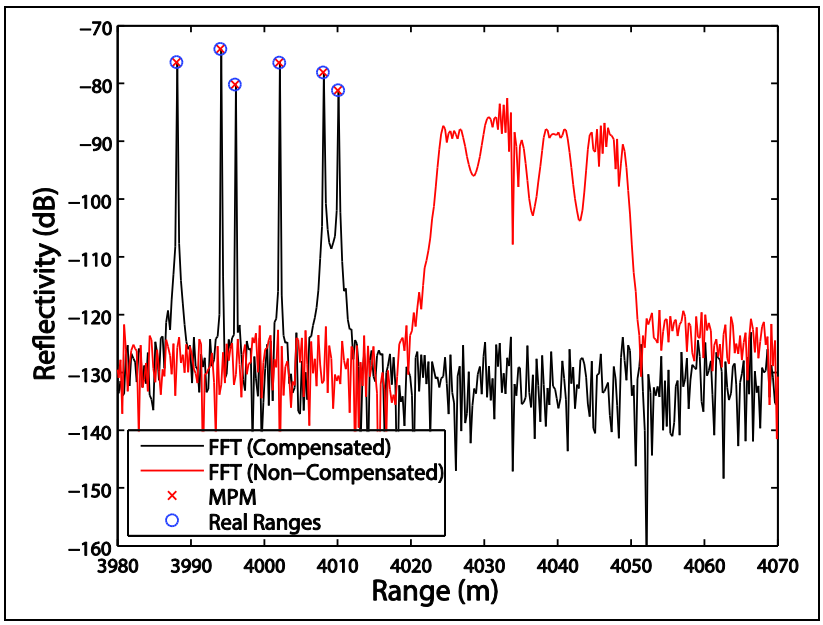

Figure 5.2: Obtained range profiles, $\theta = 93°$.

The peak points in the compensated FFT results can be distinguished from each others. Because, the differences between these ranges are greater than the range resolution $c/2B$ in the aspect angle $\theta = 93°$. However, FFT suffers from poor range resolution while the difference between two adjacent projection points is smaller than the range resolution. This issue was illustrated graphically in Figure 3 in [17].

After the range-Doppler compensation, range profiles are calculated with super resolution by MPM [37]. Then, an ISAR image has been reconstructed for each SNR value. These images can be seen in Figure 5.3. It may be said that a SNR value greater than or equal to 5 dB is sufficient for high resolution ISAR imaging. In fact, these SNR value depends on the selection of averaging factor Q. Reducing this parameter cause to increment in the required SNR. Note that Q is 180 that is used for the reconstruction of Figure 5.3. This factor yields 22.55 dB increment in the SNR value. Therefore, the SNR value should be greater than $26 - 10\log_{10} 180 = 3.45$ dB. The simulation results support this expectation.

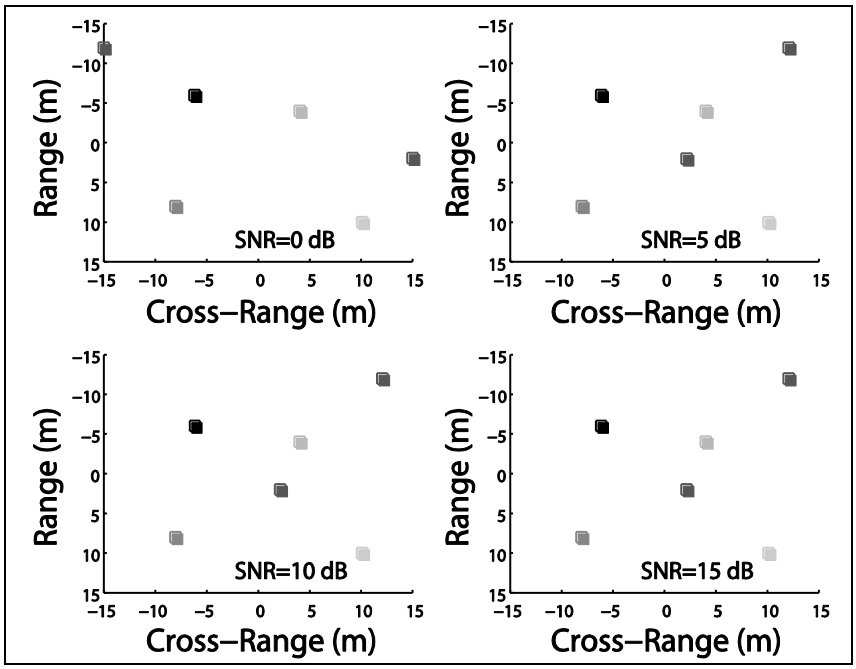

Figure 5.3: Reconstructed ISAR images.

After the reconstruction of ISAR images, each scattering center position has been optimized by using the built-in function fsolve() in MATLAB R2014a with the selection of Levenberg-Marquardt algorithm. Then, these optimized scattering centers have been used for the RCS calculation. The results can be seen in Figure 5.4 and Figure 5.5.

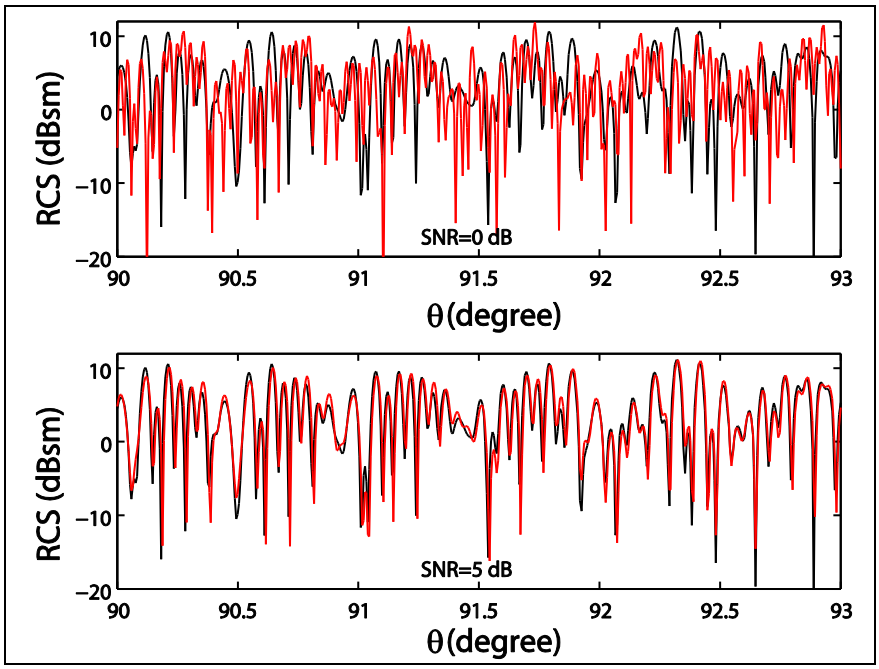

Figure 5.4: RCS graphs with 0 and 5 dB SNR values.

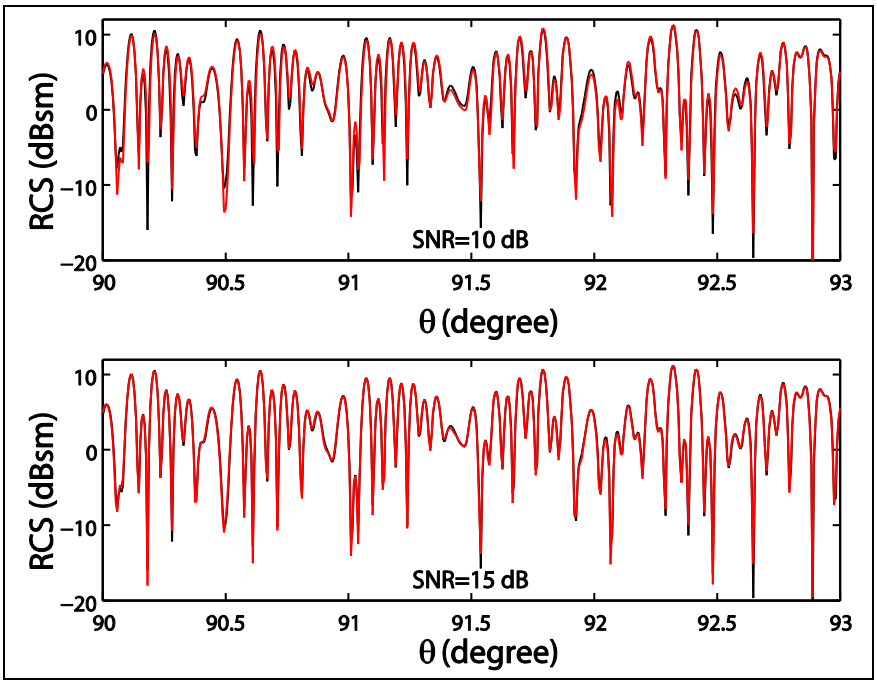

Figure 5.5: RCS graphs with 10 and 15 dB SNR values.

Again, a SNR value greater than or equal to 5 dB yields reliable RCS values. A larger averaging factor will lead to reduction in the required SNR level.

6. CONCLUSION

The PBP method was developed recently for the reconstruction of high quality SAR images by using BPMPM instead of FFT. It was emphasized by the developers of PBP that this algorithm gives super resolution in the range direction. The motivation for the present study was that the improved range resolution of the SAR images may enhance the accuracy of the tomography-based RCS extractions—a method especially developed to alleviate the far-field requirement. However, the PBP method cannot be utilized for near-field data in order to reconstruct SAR/ISAR images. This is a restriction for the usage of the PBP in terms of the tomography-based RCS extraction from near-field measurements. Hence, the IPBP method, which can be utilized for both far-field and near-field data, is introduced in this thesis. IPBP is composed of the PBP or NPBP methods, and an image segmentation algorithm for the feature extraction from the reconstructed image. In addition to the development of the IPBP, the RCS extraction performance of PBP and IPBP was studied in this work. It has been demonstrated that while PBP and NPBP produce artifacts in the cross-range dimension, IPBP advances the quality of the reconstructed image with super resolution in both the range and cross-range dimensions. This is an important enhancement on the tomography-based RCS calculation. It has been shown with simulations that the results of the IPBP supply high correlation between theoretical and extracted RCS values with synthetic data. In addition to this, using real measurement data, near-field RCS extraction results are shown to match with the far-field measurement results. Hence, the efficacy of the IPBP method for the RCS extraction from near-field measurements has been demonstrated. This is a great convenience for real life applications in order to set up SAR/ISAR measurement systems that do not satisfy the far-field conditions.

Rotating a very large target (such as a ship) to different aspect angles with a good sensitivity is difficult to perform IPBP due to the physical restrictions in a laboratory environment. Another algorithm, which facilitates reconstruction of Chirp ISAR images, is developed for moving objects. The classical range resolution of a Chirp radar is enhanced without increasing the bandwidth. In addition, there is no need to send more than one pulse to complete frequency sweep. Thus, the hardware requirements related to the bandwidth and measurement speed is alleviated. This is

an important facility to perform measurements. The simulation results are compared with the PBP and CBP results for different cases. High quality in both cross-range and range directions is obtained with the developed algorithm. These images show that the developed algorithm gives one pixel width scattering centers, which correspond to simulated points. On the other hand, PBP and CBP suffers from artifacts around the scattering centers even using point targets. Indeed, a distributed target may have some scattering centers, that are apart from each other with a distance lower than the main lobe width of the PSF for CBP or PBP. In addition, amplitude of a scattering center may be much lower than neighborhood artifacts caused by the superposition of wavefronts. Therefore, some scattering centers may not be distinguishable in the image. However, the developed Chirp ISAR algorithm doesn't require the same superposition process. Hence, the mentioned artifacts don't occur after the image reconstruction. It is a clue that the developed Chirp ISAR algorithm yields better image quality then the PBP and CBP not for only simulated scenario, but also real measurements. As another benefit, this algorithm can be used for near-field measurements, while PFA and PBP need the far-field distance. If the required $\mathrm{SNR}_r > 26 - 10\log_{10}(Q)$ condition is satisfied in the measurements, the accuracy of the developed algorithm is sufficient to predict highly reflective regions of a target at short distances. This facility decreases the difficulties related to the far-field distance and system cost in real-life applications.

In this thesis, another algorithm is introduced for the tomography-based RCS calculation for moving targets with near-field measurements. This algorithm contains a novel technique for the compensation of range-Doppler coupling. This technique facilitates a Doppler estimation with super resolution that is not bounded by the pulse width or bandwidth. This yields better accuracy than the FFT-based Doppler estimation. Thus, the developed technique can be a framework for other Doppler radar applications. Super resolution in the Doppler estimation brings high accuracy in the compensation of range-Doppler coupling. Thus, the range distortion caused by the radial velocity is alleviated sufficiently. This yields clearer ISAR images compared to the explained algorithm in Chapter 4. As another benefit, this algorithm can be used for RCS calculation of moving targets with near-field measurements. The simulation results show the efficacy of this technique.

7. FUTURE WORK

This thesis opens a new perspective by using the MPM for tomography-based RCS calculation with near-field measurements. MPM works on ill-conditioned matrices while performing SVD and eigenvalue calculations. A penetration between the singular values may lead to incorrect number of scattering centers. This will turn to reduction in the accuracy of obtained range profiles. The efficacy of this thesis under noisy signals is directly referred to [26]. However, the required SNR value to reach the Cramer-Rao bound was pointed out via empirical simulations in [26] without defining an exact analytical expression. Therefore, it will be useful to carry out a further analysis about the stability of MPM and the effect of noise to range profiles.

The Clean algorithm is a well-known tool for the scattering center extraction from a reconstructed image [3]. This algorithm needs PSF of an imaging technique in order to perform subtractions during the iterations [3]. IPBP performs back-projection in the imaging stage with point-wise range values obtained with the MPM. This leads to a PSF that is different than the traditional CBP. It will be useful to find the PSF of IPBP in order to enable the use of the Clean algorithm instead of the segmentation stages of IPBP. The accuracy of the Clean algorithm can be compared with the original IPBP by performing measurements especially for distributed targets.

Algorithms developed in Chapters 4 and 5 have not been tested with real measurements. In a future study, it will be also useful to perform this validation by using a Chirp radar or arbitrary waveform generator to address any potential concerns about the performance of these algorithms on real data. It may be observed that the results of optimization stage (see Chapter 5) may vary by changing the LMA to other methods. These differences may be more noticeable in real measurements for especially complex targets. This subject should be studied by carrying out stability analysis for different optimization techniques.

REFERENCES

[1] Knott E. F., Shaeffer J. F., Tuley M. T., (2004), “Radar Cross Section”, 2nd Edition, Scitech Publishing.

[2] Skolnik M., (2008), “Radar Handbook”, 3rd Edition, McGraw-Hill Professional.

[3] Bhalla R., Ling H., (1996), “Three-dimensional scattering center extraction using the shooting and bouncing ray technique”, IEEE Transactions on Antennas and Propagation, 44, 1445 -1453.

[4] Rigling B. D, Moses R. L., (2004), “Polar format algorithm for bistatic SAR”, IEEE Transactions on Aerospace and Electronic Systems, 40, 1147-1159.

[5] Mensa D. L., Halevy S., Wade G., (1983), “Coherent Doppler Tomography for Microwave Imaging”, Proceedings of the IEEE, 71, 254 - 261.

[6] Broquetas A., Palau J., Jofre L., Cardama A., (1998), “Spherical Wave Near-Field Imaging and Radar Cross-Section Measurement”, IEEE Transactions on Antennas and Propagation, 46, 730-735.

[7] Vaupel T., Eibert T. F., (2006), “Comparison and application of near-field ISAR imaging techniques for far-field radar cross section determination”, IEEE Transactions on Antennas and Propagation, 54, 144-151.

[8] Li S., Zhu B., Sun H., (2010), “NUFFT-based near-field imaging technique for far-field radar cross section calculation”, IEEE Antennas and Wireless Propagation Letters, 9, 550-553.

[9] Munson, D. C., O’Brien Jr., J. D., Jenkins W. K., (1983), “A tomographic formulation of spotlight-mode synthetic aperture radar”, Proceedings of the IEEE, 71, 917-925.

[10] Desai M. D., Jenkins W. K., (1992), “Convolution backprojection image reconstruction for spotlight mode synthetic aperture radar”, IEEE Transactions on Image Processing, 1, 505-517.

[11] Odendaal J. W., Joubert J., (1996), “Radar cross section measurements using near-field radar imaging”, IEEE Transactions on Instrumentation and Measurement, 45, 948-954.

[12] DeGraaf S. R., (1998), “SAR imaging via modern 2-D spectral estimation methods”, IEEE Transactions on Image Processing, 7, 729-761.

[13] Özsoy Ş., Ergin A. A., (2009), “Pencil back-projection method for SAR imaging”, IEEE Transactions on Image Processing, 18, 573-581.

[14] Qadir S. G., Fan Y., Bao-ping W., Shabbir M., Arneeb F., (2012), "ISAR Imaging of Rotating Targets Using Matrix Pencil Back-Projection Method", 9th International Bhurban Conference on Applied Sciences and Technology, 348-352, Islamabad, Pakistan, 9-12 January.

[15] Hua Y., Baqai F., Zhu Y., Heilbronn D., (1993), "Imaging of point scattering centers from step-frequency ISAR data", IEEE Transactions on Aerospace and Electronic Systems, 29, 195-205.

[16] Tulgar O., Ergin A. A., (2015), "Improved Pencil Back-Projection Method with Image Segmentation for Far-Field/Near-Field SAR Imaging and RCS Extraction", IEEE Transactions on Antennas and Propagation, 63, 2572-2584.

[17] Tulgar O., Ergin A. A., (2015), "Matrix pencil method for chirp ISAR imaging with near-field measurements", Microwave and Optical Technology Letters, 57, 1237-1242.

[18] Balanis C. A., (1989), "Advanced Engineering Electromagnetics", 2nd Edition, Wiley.

[19] Skolnik M. I., (2002), "Introduction to Radar Systems", 3rd Edition, McGraw-Hill Science/Engineering/Math.

[20] Balanis C. A., (2005), "Antenna Theory", 3rd Edition, Wiley.

[21] Knott E. F., (2006), "Radar Cross Section Measurements", 2nd Edition, Scitech Publishing.

[22] Oppenheim A. V., Schafer R. W., (2010), "Discrete-Time Signal Processing", 3rd Edition, Prentice-Hall.

[23] Ling H., Chou R. C., Lee S. W., (1989), "Shooting and Bouncing Rays: Calculating the RCS of an Arbitrary Shaped Cavity", IEEE Transactions on Antennas and Propagation, 37, 194 -205.

[24] Hua Y., Sarkar T. K., (1990), "Matrix pencil method for estimating parameters of exponentially damped/undamped sinusoids in noise," IEEE Transactions on Acoustics, Speech, and Signal Processing, 38, 814-824.

[25] Sarkar T. K., Pereira O., (1995), "Using the matrix pencil method to estimate the parameters of a sum of complex exponentials", IEEE Antennas and Propagation Magazine, 37, 48-55.

[26] Fengduo, H., Sarkar T. K., Yingbo H., (1993), "Utilization of bandpass filtering for the matrix pencil method", IEEE Transactions on Signal Processing, 41, 442-446.

[27] Otsu N., (1979), "A threshold selection method from gray-level histograms", IEEE Transactions on Systems, Man, Cybernetics, 9, 62–66.

[28] Gonzalez R. C., Woods R. E., (2007), “Digital Image Processing”, 3rd Edition, Prentice-Hall.

[29] Sarabandi K., Chiu T. C., (1996), “Optimum corner reflectors for calibration of imaging radars”, IEEE Transactions on Antennas and Propagation, 44, 1348-1361.

[30] Doerry A. W., (2008), “Reflectors for SAR performance testing”, Sandia Report SAND2008-0396, Unlimited Release, Sandia National Laboratories, USA.

[31] Meta A., Hoogeboom P., Ligthart L. P., (2007), “Signal processing for FMCW SAR”, IEEE Transactions on Geoscience and Remote Sensing, 45, 3519-3532.

[32] Lin A., Ling H., (2007), “Doppler and direction-of-arrival (DDOA) radar for multiple-mover sensing”, IEEE Transactions on Aerospace and Electronic Systems, 43, 1496-1509.

[33] Hua Y., Sarkar T. K., (1991), “On SVD for estimating generalized eigenvalues of singular matrix pencil in noise”, IEEE Transactions on Signal Processing, 39, 892-900.

[34] Yilmazer N., Koh J., Sarkar T. K., (2006), “Utilization of a unitary transform for efficient computation in the matrix pencil method to find the direction of arrival”, IEEE Transactions on Antennas and Propagation, 54, 175-181.

[35] Hwang S., Burintramart S., Sarkar T. K., Best S. R., (2006), “Direction of arrival (DOA) estimation using electrically small tuned dipole antennas”, IEEE Transactions on Antennas and Propagation, 54, 3292-3301.

[36] Muñoz-Ferreras J., Gómez-García R., (2014), “Beyond the stop-and-go assumption in pulse-Doppler radar sensors”, IEEE Sensors Journal, 14, 3046-3051.

[37] Tulgar O., Ergin A. A., (2016), “Matrix pencil method for estimating radar cross section of moving targets with near-field measurements”, Microwave and Optical Technology Letters, 58, 471-476.

[38] Nocedal J., Wright S. J., (1999), “Numerical Optimization”, 2nd Edition, Springer.

[39] Marquardt D. W., (1963), “An Algorithm for Least-Squares Estimation of Nonlinear Parameters”, SIAM Journal of the Society for Industrial and Applied Mathematics, 11, 431–441.

[40] Seber G. A. F., Wild C. J., (1989), “Nonlinear Regression”, 1st Edition, Wiley.

[41] Moré J. J., (1977), “The Levenberg-Marquardt Algorithm: Implementation and Theory”, Numerical Analysis, ed. G. A. Watson, Lecture Notes in Mathematics, 630, 105–116, Springer.

BIOGRAPHY

Okyanus TULGAR was born in Istanbul, Turkey, in 1986. He received the B.Sc. and the M.Sc. degrees in electronics engineering from the Gebze Technical University, Gebze, Kocaeli, Turkey, in 2010 and 2013, respectively. He has been a doctoral student in Gebze Technical University, Graduate School of Natural and Applied Sciences, Department of Electronic Engineering since 2013.

Between 2011- mid. 2015, he was a research assistant in the Electronics Engineering Department and researcher at ASEMLAB, Gebze Technical University. Since mid. 2015, he has been a senior researcher in the Scientific and Technological Research Council of Turkey (TUBITAK). He is interested in the stealth technologies, SAR/ISAR imaging, RCS measurements or calculations, RCS reduction techniques, EM wave propagation, computational electromagnetic, digital signal and image processing.

APPENDICES

Appendix A: Published Journals From Doctoral Thesis

Tulgar O., Ergin A. A., (2015), “Improved Pencil Back-Projection Method with Image Segmentation for Far-Field/Near-Field SAR Imaging and RCS Extraction”, IEEE Transactions on Antennas and Propagation, 63, 2572-2584.

Tulgar O., Ergin A. A., (2015), “Matrix pencil method for chirp ISAR imaging with near-field measurements”, Microwave and Optical Technology Letters, 57, 1237-1242.

Tulgar O., Ergin A. A., (2016), “Matrix pencil method for estimating radar cross section of moving targets with near-field measurements”, Microwave and Optical Technology Letters, 58, 471-476.